Spectral Decomposition for Graded Multi-Scale Topology Optimization

Tej Kumar[a], Saketh Sridhara[a,1], Bhagyashree Prabhune[a,1], Krishnan Suresh[a,*]

[a]*Department of Mechanical Engineering, University of Wisconsin-Madison, Madison, WI, USA*

Abstract

Multi-scale topology optimization (MTO) is exploited today in applications that require designs with large surface-to-volume ratio. Further, with the advent of additive manufacturing, MTO has gained significant prominence. However, a major drawback of MTO is that it is computationally expensive. As an alternate, graded MTO has been proposed where the design features at the smaller scale are graded variations of a single microstructure. This leads to significant reduction in computational cost, while retaining many of the benefits of MTO.

Graded MTO fundamentally rests on interpolation of elasticity matrices. The *direct* method of interpolation used today unfortunately does not guarantee positive-definiteness of the resulting matrices. Consequently, during the graded MTO algorithm the strain energy may become negative and non-physical.

In this paper, we propose a simple but effective *spectral decomposition*-based approach which guarantees positive-definite elasticity matrices. The proposed method relies on a spectral (eigen) decomposition of instances of the elasticity matrices, followed by regression of eigenvalues and interpolation of eigenvector orientations. The resulting elasticity matrix can then be used for stable optimization. The direct and spectral decomposition methods are compared here for robustness, accuracy and speed, through several numerical experiments.

Keywords: Spectral Decomposition, Elasticity Matrix, Lattice, Multi-scale Topology Optimization, Asymptotic Homogenization

1. Introduction

Topology optimization is a strategy for distributing material within a design domain to optimize an objective, such as compliance, under a set of constraints [1, 2]. Various methods of topology optimization have been proposed; these include solid isotropic material with penalization (SIMP) [3], rational approximation of material properties (RAMP) [4], homogenization [5, 6], level-set [7, 8], evolutionary scheme [9, 10], morphable components [11], and topological sensitivity based methods [12, 13]. These methods typically

*Corresponding author

Email addresses: tkumar3@wisc.edu (Tej Kumar), ssridhara@wisc.edu (Saketh Sridhara), bprabhune@wisc.edu (Bhagyashree Prabhune), ksuresh@wisc.edu (Krishnan Suresh)

[1]These authors contributed equally to this work.

lead to a single-scale design where the geometric features are all at a single length scale. For example, for the L-Bracket problem posed in Fig. 1, single-scale optimization leads to the topology in Fig. 2a.

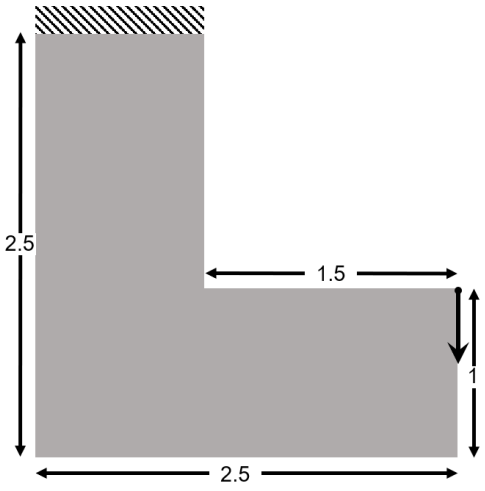

Figure 1: L-Bracket design problem.

In contrast, in multi-scale topology optimization (MTO) [14], geometric features are computed at two or more length scales, separated by at least an order of magnitude [15]; Fig. 2b illustrates a two-scale MTO. MTO designs exhibit unique characteristics such as large surface-to-volume ratio, excellent resilience, etc. This has led to a wide range of applications [16, 17] including energy absorption [18], heat exchangers [19], and biomedical applications [20]. MTO methods include clustering [21, 22], kriging [23], multi-material [24], etc. The advent of additive manufacturing has further spurned research in MTO [16].

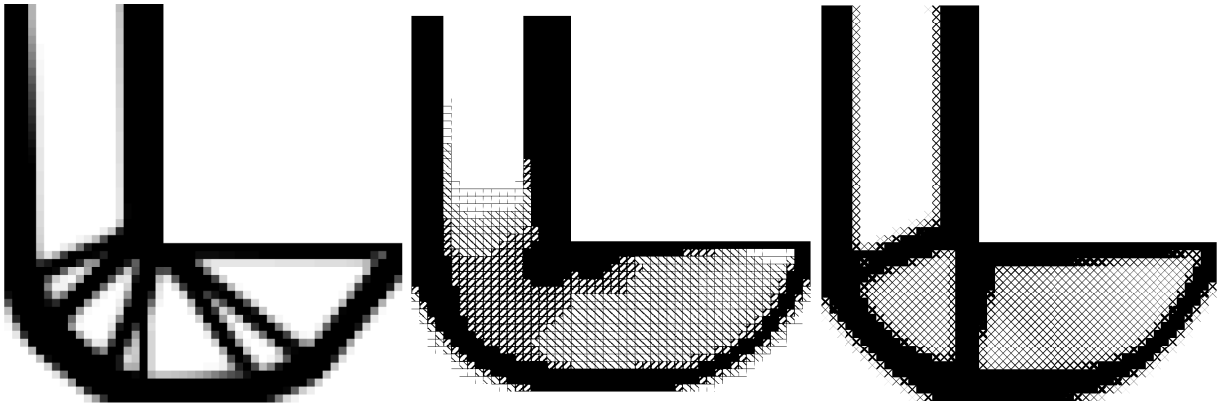

(a) (b) (c)

Figure 2: Various types of TO for an L-bracket: (a) single-scale TO using SIMP (b) multi-scale TO using density clustering (reproduced from [22]), and (c) graded MTO using an X-shaped microstructure.

However, one of the challenges in MTO is the high computational cost since one must numerically evaluate various microstructures (topologies at the smaller length scale) during each step of the optimization process [14, 21, 22]. To address this challenge, researchers have proposed use of microstructures that are

simple graded variations of a single microstructural topology [15, 25, 19]. This is referred as graded MTO and illustrated in Fig. 2c, where, graded variations of an X-shaped microstructure is used everywhere. It leads to a significant reduction in computational cost [26], while retaining many of the benefits of MTO.

Graded MTO methods fundamentally rely on the concept of *elasticity-matrix-interpolation* [27]. To illustrate, we consider a typical thickness based gradation illustrated in Fig. 3. Note that, to ensure smoothness between neighboring cells, other types of gradation are also possible such as cosine functions for rectangular-void microstructures [28], level-set contours [29, 30], optimized microstructures [31], etc. Since explicitly computing the effective elasticity matrix for every instance of the microstructure is expensive, one typically pre-computes the elasticity matrix (six scalars in 2D) at a finite number of instances. Then, during optimization, the matrix quantities are interpolated [32, 15, 33], using, for example, polynomial curve fitting. This makes graded MTO highly efficiently. However, the interpolated matrices may lose their positive definiteness [32], leading to non-physical negative strain-energy during the graded MTO algorithm [34].

Figure 3: Graded variations of an X-shaped microstructure.

In this paper, we propose a *spectral decomposition (SD)* based curve fitting of the elasticity matrices. Specifically, the elasticity matrices are pre-computed for a finite number of instances (as before). Then, a spectral (eigen) decomposition is carried out for all these instances [35]. Finally, during the optimization, instead of directly fitting the matrices, we propose to interpolate the eigenvalues and orientation angles corresponding to eigenvectors. We demonstrate that this not only ensures positive definiteness of the resulting matrices, but also aids in identification of inherent symmetry of the microstructure.

2. Literature Review and Background

In this section, the graded MTO problem is posed, followed by a description of a typical graded MTO algorithm.

2.1. Problem formulation

The graded MTO problem can be mathematically posed as:

$$\underset{\rho(\boldsymbol{x})}{\text{minimize}} \quad J(\rho, \boldsymbol{u}) \tag{1a}$$

$$\text{subject to} \quad \boldsymbol{K}(\boldsymbol{C}(\rho))\,\boldsymbol{u} = \boldsymbol{f}, \tag{1b}$$

$$C_{ij}(\rho) = p_{ij}(\rho; \boldsymbol{P}), \tag{1c}$$

$$V(\rho) \le V^*, \tag{1d}$$

$$\underline{\rho} \le \rho \le \overline{\rho} \tag{1e}$$

where the density design variable $\rho(\boldsymbol{x})$ must be determined to minimize an objective function J, such as compliance $J = \boldsymbol{f}^{\mathsf{T}}\boldsymbol{u}$, while satisfying one or more constraints, such as a volume constraint given by Eqn. 1d. Eqn. 1e provides $\underline{\rho}$ and $\overline{\rho}$ as the lower and upper bounds for the design variables. The displacement vector $\boldsymbol{u}$ is computed via the governing Eqn. 1b where $\boldsymbol{K}$ is the stiffness matrix and $\boldsymbol{f}$ is the force vector. A critical aspect of graded MTO is Eqn. 1c where the interpolation functions $p_{ij}(\rho; \boldsymbol{P})$ (often polynomials) are pre-computed based on a set of user-defined parameters $\boldsymbol{P}$; see discussion below. This is in contrast to classic SIMP, where the polynomials are trivially defined via $C_{ij}(\rho) = C^0_{ij}\rho^p$ where p is the penalty parameter.

2.2. Review of Graded MTO Algorithm

As mentioned earlier, the MTO problem is solved in two phases. In the first phase, the interpolation functions $p_{ij}(\rho; \boldsymbol{P})$ are constructed. The user-defined parameters $\boldsymbol{P}$ include: (a) the microstructural topology τ, (b) the number of samples $(s{+}1)$ to be used for regression, and (c) the type and degree d of fitting functions. In the second phase, the interpolation is used to carry out the actual optimization. Each of these steps is described below. For simplicity, it is assumed that the base material is isotropic, i.e., the Young's modulus and Poisson's ratio are assumed to be given.

(1) Choosing a Microstructural Topology: The first step is to choose a microstructural topology. Microstructures with straight members, such as the ones in Fig. 4, have been used extensively [36, 17, 37, 38]. A classification of these microstructures is discussed in [39]. Inclusion of curved members has shown to increase energy absorption [40]. Optimized microstructural topologies have also been proposed [31, 41, 42]. The remainder of this paper is independent of the chosen topology. The only assumption made here is that, for each value of $0 \le \rho \le 1$, one can assign a thickness to the topology (see Fig. 3) such that the volume fraction of the resulting structure is ρ.

(2) Sampling and Homogenization: Once the topology is chosen, the next step is to generate a finite number of microstructure instances, typically eight to ten such instances [43], [44], each corresponding to a unique value of ρ_k; typical samples based on an X-shaped topology are illustrated in Fig. 3. Then, for each of these samples, the effective elasticity matrix for each is computed using homogenization techniques. In this paper, we shall rely on asymptotic homogenization (AH) [43] for computing the effective elasticity matrices.

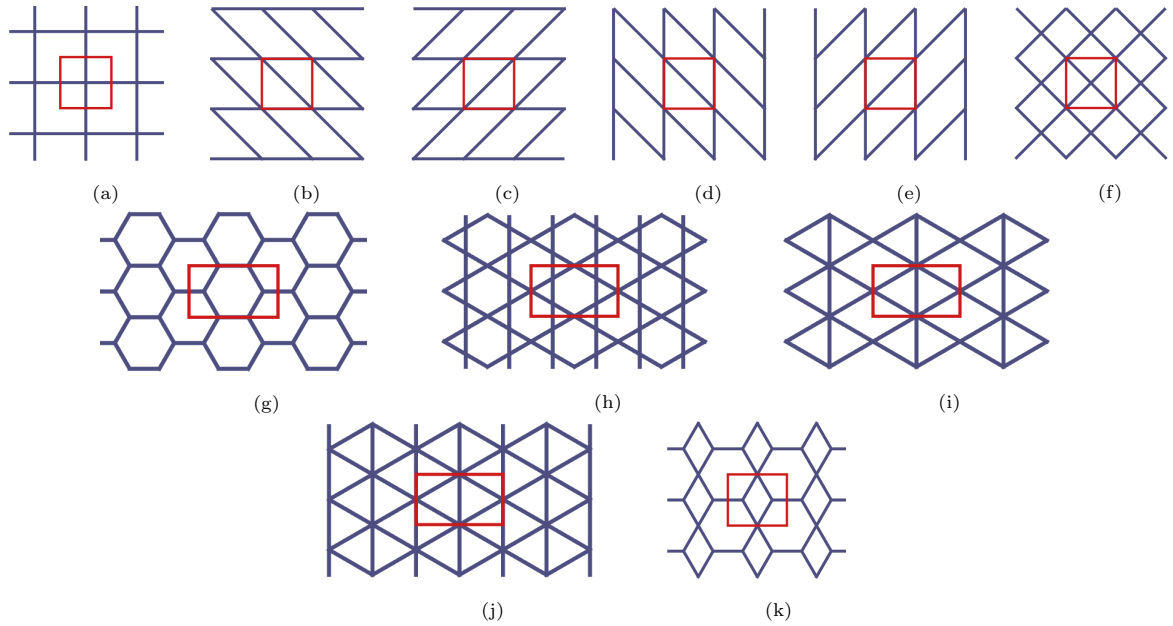

Figure 4: Various types of two-dimensional microstructures; red box highlights a repeating unit cell.

The characteristics of AH [43] include: (1) it has no topology limitation and is valid for values of ρ_k, (2) it supports stress computation, (3) it agrees well with experimental results, but (4) it may be inaccurate if the assumption of periodicity breaks down, e.g. near the boundaries. AH is performed numerically using finite element analysis [45] to compute the elasticity matrices $\boldsymbol{C}(\rho_k)$.

(3) Curve fitting: The next step is to choose a curve fitting strategy; this must satisfy two requirements:

1. Fit the data 'well enough', with a high R^2 value [46].
2. The interpolated matrices $\boldsymbol{C}(\rho)\ \forall\ \rho \in (0,1]$ must be positive definite.

Various fitting functions have been proposed that meet the first requirement. Jansen et al. [47] and Watts et al. [48] describe a piece-wise linear interpolation for square and cubic microstructures. A cubic polynomial has been used in Wu et al. [49]. Quartic polynomials have been demonstrated in [44]. Fourth order polynomials without the cubic term have been used by [50, 51], and a degree-5 polynomial in [52]. A combination of linear interpolation and polynomial fit is demonstrated in Wang et al. [15]. Non-polynomial curve fittings have also been employed as; for example, an exponential fit in [53], and a cubic spline interpolation scheme in [54]. However, these schemes do not guarantee that the interpolated matrices are positive definite (see discussion below).

(4) Optimization: Once the fitting function has been defined, graded MTO is performed along the lines of classic SIMP [1, 2]. The design domain, boundary conditions and a finite element mesh are defined. The density variable ρ defined over each finite element is also initialized. The effective elasticity matrix for all elements is computed via the fitting function. This is followed by finite element analysis and sensitivity computation. The element densities are updated and the process is repeated until convergence.

2.3. Numerical Challenges with Curve Fitting

The two main challenges with the current MTO methods are: (1) possible loss of positive definiteness of $\boldsymbol{C}$ matrix and (2) non-monotonicity of fitting functions. Positive-definiteness is required to ensure that the strain energy remains positive [5], while monotonicity ensures stability of the algorithm [55]. The fitting strategies discussed above do not guarantee that the interpolated matrices will be positive-definite [56] or monotonic. For example, consider Fig. 5 where a quartic polynomial [57] is used to fit various components of the $\boldsymbol{C}$ matrix. Although the sampled components are all positive, the interpolated component C_{12} is negative at ρ = 0.0302 as illustrated (and the curve is non-monotonic). Note that, even with positive diagonal components of $\boldsymbol{C}$, the positive-definiteness is not guaranteed.

These challenges can be handled in two ways: (1) as special cases, by omitting an order of the fitting function [57], [50], or by using a linear scheme at lower density regions [15], or (2) enforcing constraints that ensure positive definiteness. The first strategy of omitting an order term (such as the third order term in a fourth order polynomial fitting function) does not generalize well to all types of microstructure, and such an omission impacts the R^2 value of the fit. Using a linear scheme at lower density regions works well for isotropic and orthogonal-isotropic microstructures. However, it is observed that for generally anisotropic microstructures such as the Z type, instabilities arise at densities as high as $\rho = 0.4$. Therefore, the linear scheme would need to be extended to higher density regions, thereby significantly compromising the fit. Further, it has been observed that additional constraints will result in a loss in accuracy of the fit [58]. Additionally, ensuring positive-definiteness for an anisotropic microstructure involves interpolating six independent terms of the matrix, and ensuring positive-definiteness at all values of ρ; this is non-trivial when imposed directly via the matrix components due to the strong coupling between the components of the elasticity matrix.

To address these shortcomings, we propose a curve fitting strategy based on spectral decomposition of the elasticity matrix that guarantees positive-definiteness of the elasticity matrix $\forall\ \rho \in (0,1]$.

3. Proposed Strategy

In this section, we propose a method of curve fitting based on the spectral decomposition or eigendecomposition, of the sampled elasticity matrices to ensure positive definiteness of the interpolated elasticity matrices, leading to a modification of Eqn. 1c, as explained below.

3.1. Backrground

Spectral decomposition of the elasticity matrix was first discussed by Lord Kelvin [59] in 1856. Later, in the last decade of 20th century, the algebraic representation of the elasticity matrix in spectral form was applied to anisotropic elasticity by Mehrabadi and Cowin [60], Sutcliffe [61], Theocaris and Philippidis [62, 63]. Theocaris and Sokolis [64, 65, 66] studied in detail the spectral decomposition for various symmetries such as monoclinic, tetragonal, hexagonal media and anisotropic plates, emphasizing the importance of

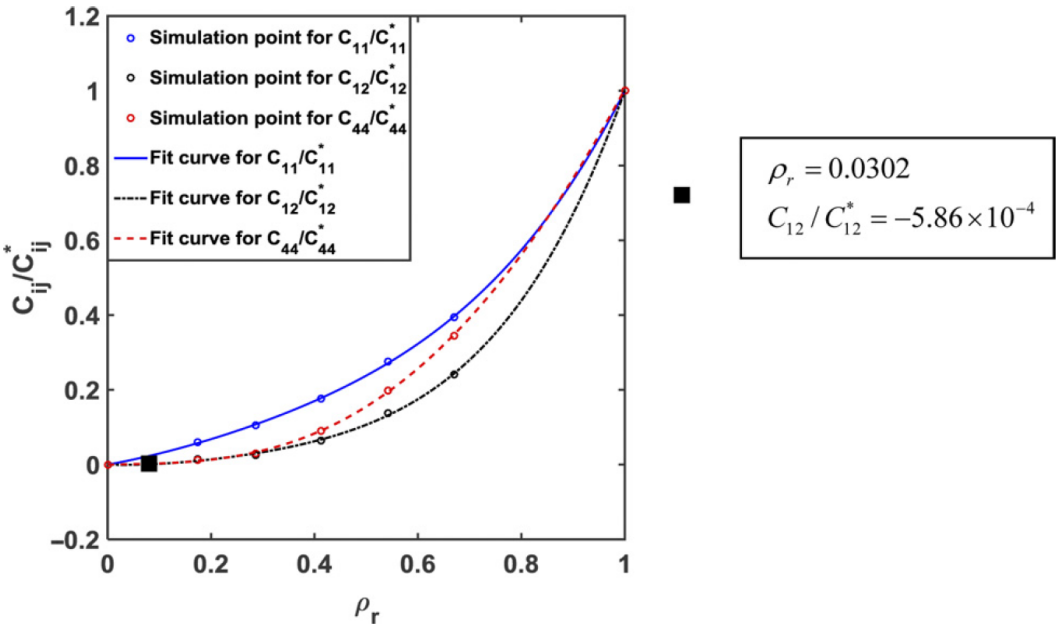

Figure 5: Polynomial interpolation of elasticity matrix components can lead to non-monotonicity; adapted from Cheng et al. [57].

eigenangles [63]. More recently, spectral decomposition of elasticity matrix has been applied in topology optimization. For instance, Jantos et al. [67, 68] applied spectral decomposition to describe local orientation of the base anisotropic material in the context of continuous fiber angle optimization. Spectral decomposition has been used in free material design [69] in which the spatial distribution of elasticity matrix in the spectral form is optimized [70, 71]. Liu and Shapiro [35] applied it to determine the material orientation in the synthesis of a 2-scale structure. However, to the best of our knowledge, spectral decomposition has not been employed to enforce the positive definiteness of the interpolated elasticity matrices.

3.2. Spectral decomposition of effective elasticity matrices

To describe the underlying concept, consider a 2-D anisotropic graded-microstructure without symmetry, whose effective elasticity matrix $\boldsymbol{C}$ can be computed numerically. Using Voigt notation, $\boldsymbol{C}$ can be represented as a symmetric 3×3 positive definite matrix. Further, let $\boldsymbol{C}_k$ be an instance of $\boldsymbol{C}$ at ρ_k. Let $\lambda_k^{(i)}$ and $\boldsymbol{v}_k^{(i)}$, $i = 1, 2, 3$ be the eigenvalues and eigenvectors of $\boldsymbol{C}_k$, i.e., $\boldsymbol{C}_k \boldsymbol{v}_k^{(i)} = \lambda_k^{(i)} \boldsymbol{v}_k^{(i)}$. Let $\boldsymbol{\Lambda}_k$ be the diagonal matrix of eigenvalues $\lambda_k^{(i)}$ and $\boldsymbol{V}_k$ be a matrix with the eigenvectors as its columns. Then, by definition,

$$\boldsymbol{C}_k = \sum_{i=1}^{3} \lambda_k^{(i)} \boldsymbol{v}_k^{(i)} \otimes \boldsymbol{v}_k^{(i)} = \boldsymbol{V}_k \boldsymbol{\Lambda}_k \boldsymbol{V}_k^{\mathsf{T}}. \tag{2}$$

where $\otimes$ represents the dyadic or the outer product.

Since $\boldsymbol{C}_k$ is symmetric positive definite, the eigenvalues $\lambda_k^{(i)}$ are real and positive, and the eigenvectors are orthonormal [72]. The objective now is to develop a scheme to fit functions using eigenvalues and eigenvectors of the sampled matrices.

3.3. Curve fitting for effective elasticity matrices

Given the sampled eigenvalues $\lambda_k^{(i)}$, each of the three distinct eigenvalues can be interpolated as:

$$\lambda^{(i)}(\rho) = q^{(i)}(\rho; \boldsymbol{P}); \quad i = 1, 2, 3 \tag{3}$$

where $\boldsymbol{P}$ are the user-defined parameters discussed earlier. One can also express this as:

$$\Lambda_{ii}(\rho) = q^{(i)}(\rho; \boldsymbol{P}); \quad i = 1, 2, 3 \tag{4}$$

The fitting functions $q^{(i)}$ should be such that the eigenvalues are positive $\forall \rho \in (0,1]$. This is achieved by imposing non-negativity constraint on the coefficients of $q^{(i)}$. Note that the fitting functions are independent, and therefore imposition of these constraints is trivial.

In order to interpolate the eigenvectors, we describe every instance $\boldsymbol{V_k}$ about a reference basis $\boldsymbol{B}_\mathrm{R}$ using three angles $(\alpha_k, \beta_k, \gamma_k)$, as follows:

$$\boldsymbol{V}_k = \boldsymbol{R}(\alpha_k, \beta_k, \gamma_k)\boldsymbol{B}_\mathrm{R}. \tag{5}$$

where

$$\boldsymbol{R} = \begin{bmatrix} \cos\alpha_k \cos\beta_k & \cos\alpha_k \sin\beta_k \sin\gamma_k - \sin\alpha_k \cos\gamma_k & \cos\alpha_k \sin\beta_k \sin\gamma_k + \sin\alpha_k \sin\gamma_k \\ \sin\alpha_k \cos\beta_k & \sin\alpha_k \sin\beta_k \sin\gamma_k + \cos\alpha_k \cos\gamma_k & \sin\alpha_k \sin\beta_k \cos\gamma_k - \cos\alpha_k \sin\gamma_k \\ -\sin\beta_k & \cos\beta_k \sin\gamma_k & \cos\beta_k \cos\gamma_k \end{bmatrix} \tag{6}$$

Typically, the first eigenvector matrix $\boldsymbol{V}_1$ corresponding to the lowest density is taken as the reference $\boldsymbol{B}_\mathrm{R}$; please see subsection 4.2. A method to compute the three angles, given $\boldsymbol{V_k}$ and $\boldsymbol{B}_\mathrm{R}$ using Givens matrices [73], is described later. Finally, given finite number of instances α_k, β_k and γ_k, we construct interpolating splines $r(\rho; \boldsymbol{P}), s(\rho; \boldsymbol{P})$ and $t(\rho; \boldsymbol{P})$ for these three angles respectively. A spline interpolation is preferred over polynomial regression for an improved accuracy of fitting function over non-monotonic orientation angle data as explained in section 4.3. This results in an interpolated eigenvector matrix:

$$\boldsymbol{V}(\rho) = \boldsymbol{R}\left(r(\rho; \boldsymbol{P}), s(\rho; \boldsymbol{P}), t(\rho; \boldsymbol{P})\right)\boldsymbol{B}_\mathrm{R}. \tag{7}$$

Finally, one can construct the interpolated elasticity matrix:

$$\boldsymbol{C}(\rho) = \boldsymbol{V}(\rho)\boldsymbol{\Lambda}(\rho)\boldsymbol{V}^\mathsf{T}(\rho). \tag{8}$$

In summary, in the proposed strategy, Eqn. 1c is replaced by Eqn. 8. It will be shown that both the requirements of the interpolation strategy – (a) high R^2 value for the fitting functions, and (b) positive-definiteness of the interpolated elasticity matrix $\boldsymbol{C}(\rho)$ $\forall$ $\rho \in (0,1]$ – are seamlessly satisfied with the proposed strategy based on spectral decomposition. For conciseness, we will drop the term $\boldsymbol{P}$ representing user-defined parameters from hereon.

4. Implementation

The implementation details on sampling, spectral decomposition and curve fitting are explained in this section. Other essential concepts including finite element discretization, sensitivity analysis, filtering [74] to avoid checkerboard patterns [75], use of optimality criteria [76], etc. are discussed, for example, in [1, 76].

4.1. Sampling and Asymptotic Homogenization

Given the line topology of a microstructure (see Fig. 6a), one can assign a thickness t to construct the microstructure. Further, there is direct correspondence between the thickness t, and the effective density (fill-ratio) ρ. Thus, there are two strategies for sampling microstructures at different densities: (1) create microstructures with sampled thicknesses t_k and compute the resulting densities ρ_k, or (2) select a uniformly sampled set of densities ρ_k and back-calculate (via a simple binary search) the thicknesses t_k. In this paper, we adopt the latter as illustrated in Fig. 6b since it guarantees a more uniform density distribution. Further, without a loss of generality, we will assume 10 samples of ρ_k between $\rho_1 = \rho_{\min}$ and $\rho_{10} = 1.0$ (inclusive). The value of $\rho_{\min}$ is chosen to ensure that the corresponding thickness is at least two times the finite element size.

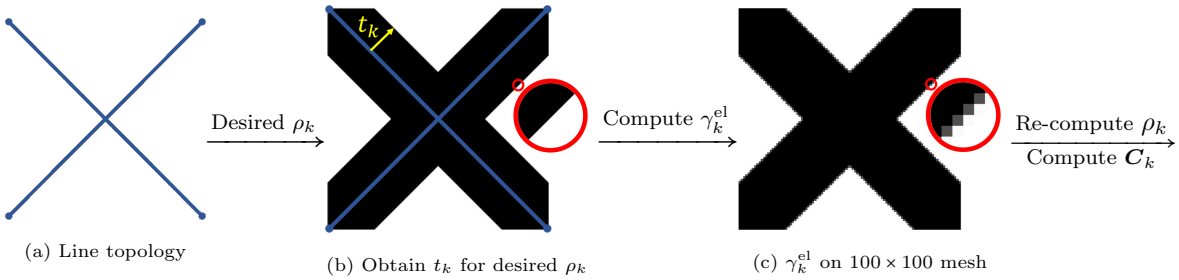

(a) Line topology (b) Obtain t_k for desired ρ_k (c) γ_k^{el} on 100×100 mesh

Figure 6: For a given microstructure topology, (1) a thickness t_k is calculated for a desired ρ_k, (2) γ_k^{el} is then determined for each element, and (3) a corrected ρ_k is computed along with $\boldsymbol{C}_k$.

Once the thickness has been computed, i.e., the microstructure has been constructed, we discretize the domain using bilinear quadrilateral elements. Specifically, a microstructure of aspect ratio η (i.e., size $\eta \times 1$) is discretized using $100\eta \times 100$ quadrilateral elements. The next step is to compute the (fill) density γ_k^{el} of each micro-element. Note that the symbol γ is used to refer to densities at the micro-scale, while ρ is used to refer to densities at the macro-scale. Thus, here, the superscript 'el' refers to the finite elements at the micro-scale. To find γ_k^{el}, the signed distance of each node from the microstructure boundary is computed. Then, the elements are classified as completely inside ($\gamma_k^{\text{el}} = 1$), partially inside ($0 < \gamma_k^{\text{el}} < 1$), or completely outside ($\gamma_k^{\text{el}} = 0$), depending on the sign of the distance function at the four associated nodes. Further, for elements that are partially inside, the four signed distance values can be used to compute γ_k^{el} via a local contour extraction; see Fig. 6c. Given γ_k^{el}, the elastic modulus of each micro-element is determined via

$$E_k^{\text{el}} = E_0 \gamma_k^{\text{el}} \tag{9}$$

where $E_0 = 1$. Then, asymptotic homogenization (AH) [45] is carried out to obtain the effective elasticity matrix $\boldsymbol{C}_k$ of the microstructure at that sample. Finally, to correct for numerical errors, we also re-compute ρ_k (see Fig. 6c) for the microstructure via:

$$\rho_k = \frac{\sum_{\text{el}} \gamma_k^{\text{el}}}{\sum_{\text{el}} 1} \tag{10}$$

4.2. Spectral Decomposition

For each instance $\boldsymbol{C}_k$, the eigenvalue matrix $\boldsymbol{\Lambda}_k$ and eigenvector matrix $\boldsymbol{V}_k$ are computed. The first eigenvector matrix $\boldsymbol{V}_1$ corresponding to $\rho_1 = \rho_{\min}$ is taken as the reference $\boldsymbol{B}_{\text{R}}$, referred to earlier in Eqn. 5. Thus, the rotation matrix for any instances obtained via:

$$\boldsymbol{R}(\alpha_k, \beta_k, \gamma_k) = \boldsymbol{V}_k \boldsymbol{V}_1^{-1} \tag{11}$$

The rotation matrix is then decomposed into three right-handed rotation matrices about the three coordinate axes as

$$\boldsymbol{R}(\alpha_k, \beta_k, \gamma_k) = \boldsymbol{R}_z(\alpha_k)\boldsymbol{R}_y(\beta_k)\boldsymbol{R}_x(\gamma_k) \tag{12}$$

where the three rotation matrices are

$$\boldsymbol{R}_z(\alpha_k) = \begin{bmatrix} \cos\alpha_k & -\sin\alpha_k & 0 \\ \sin\alpha_k & \cos\alpha_k & 0 \\ 0 & 0 & 1 \end{bmatrix} \qquad \boldsymbol{R}_y(\beta_k) = \begin{bmatrix} \cos\beta_k & 0 & \sin\beta_k \\ 0 & 1 & 0 \\ -\sin\beta_k & 0 & \cos\beta_k \end{bmatrix} \qquad \boldsymbol{R}_x(\gamma_k) = \begin{bmatrix} 1 & 0 & 0 \\ 0 & \cos\gamma_k & -\sin\gamma_k \\ 0 & \sin\gamma_k & \cos\gamma_k \end{bmatrix}$$

The three angles $\alpha_k, \beta_k, \gamma_k$ are obtained using Givens rotation as described in Algorithm 1 [77]. The above process is repeated for all samples ρ_k.

Algorithm 1 Orientation angle computation using Givens rotation

1: Set $\boldsymbol{R} = \boldsymbol{R}(\alpha_k, \beta_k, \gamma_k)$
2: $\alpha_k = \arctan(R_{21}/R_{11})$
3: $\boldsymbol{S} = \boldsymbol{R}_z(\alpha_k)^{\mathsf{T}}\boldsymbol{R}$
4: $\beta_k = \arctan(-S_{31}/S_{11})$
5: $\boldsymbol{T} = \boldsymbol{R}_y(\beta_k)^{\mathsf{T}}\boldsymbol{S}$
6: $\gamma_k = \arctan(T_{32}/T_{22})$

4.3. Curve Fitting

Next, we consider fitting the sampled eigenvalues and rotation angles. Special care must be taken in handling crossing-over of eigenvalues. For example, observe in Fig. 7a that the first and second eigenvalue cross-over at $\rho_k = 0.8$ due to incorrect labeling. To avoid this, the dot-product of consecutive eigenvectors is used to ensure proper labeling, as illustrated in Fig. 7b.

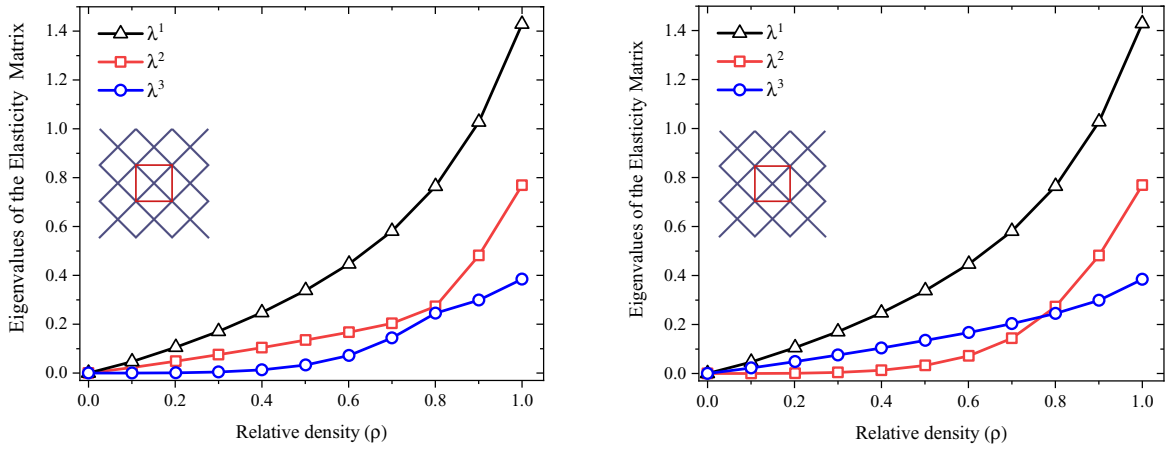

(a) (b)

Figure 7: Ordering eigenvalues of an X-shaped microstructure by (a) numerically sorting the eigenvalues, and (b) by using the direction of eigenvectors.

For regression of the three eigenvalues, homogeneous polynomials, i.e., polynomials with the constant term being zero, of degree of d are used here:

$$q^{(i)}(\rho) = \sum_{j=1}^{d} q_j^{(i)} \rho^j \qquad i = 1, 2, 3 \tag{13}$$

The degree d is varied between 1 and 10 in the numerical experiments. Further, to ensure positive-definiteness, non-negativity is enforced on all the coefficients $q_j^{(i)}$. Here, MATLAB's linear least square solver `lsqlin` is used for regression. Since the derivative(s) of the fitting functions $q^{(i)}(\rho)$ are polynomials with positive coefficients, we have the following three properties:

$$\text{Positivity:} \qquad q^{(i)}(\rho) > 0 \qquad \forall \rho \in (0, 1] \tag{14a}$$

$$\text{Monotonicity:} \qquad \frac{\mathrm{d}q^{(i)}(\rho)}{\mathrm{d}\rho} > 0 \qquad \forall \rho \in (0, 1] \tag{14b}$$

$$\text{Convexity:} \qquad \frac{\mathrm{d}^2 q^{(i)}(\rho)}{\mathrm{d}\rho^2} \geq 0 \qquad \forall \rho \in (0, 1] \tag{14c}$$

For interpolating the orientation angles given in Eqn. 7, we employ here a C^2 continuous cubic spline over each interval $[\rho_k, \rho_{k+1}]$, rather than polynomials since the orientation angles are non-monotonic. For example, the orientation angle $r(\rho)$ at any density ρ between two instances ρ_i and ρ_{i+1} is interpolated as follows:

$$r(\rho) = a_i(\rho - \rho_i)^3 + b_i(\rho - \rho_i)^2 + c_i(\rho - \rho_i) + d_i \qquad \forall\ \rho \in [\rho_i, \rho_{i+1}] \tag{15}$$

where the four coefficients a_i, b_i, c_i and d_i are determined using standard cubic-spline fitting procedures.

5. Consistency in Fitting

Although, in the most generic case, we will need a total of 6 interpolating functions, if the microstructure exhibits symmetry (example, isotropic), fewer fitting functions are needed. Here, we highlight the consistency between the number of independent fitting functions needed for a given microstructure, and the number of independent components in the corresponding elasticity matrix. In particular we consider four microstructures, each representing a particular symmetry group: (1) isotropic Kagome microstructure, (2) orthogonal-isotropic cross-shaped microstructure, (3) orthotropic mixed-triangular microstructure, and (4) anisotropic Z-shaped microstructure. It is well known that the number of independent components in the elasticity matrix for each of these microstructures is 2, 3, 4 and 6 respectively. For each of these microstructures, the eigenvalue and orientation angle fitting functions are generated, and observations are made below.

5.1. Isotropic Kagome microstructure

First, we consider the isotropic Kagome microstructure. The spectral decomposition method generates three eigenvalues and three orientation angles. Fig. 8 illustrates the fitting functions for these eigenvalues and orientation angles. Although, three distinct eigenvalue curves are shown, one can show that the third eigenvalue is half of the second eigenvalue; see Appendix B. Further, the eigenvectors for isotropic microstructures are always constant (see Appendix A and Appendix B), i,e., interpolation of the orientation angles is not required. In summary, the total number of linearly independent fitting functions is two. This is consistent with the number of independent elastic constants for isotropic microstructures.

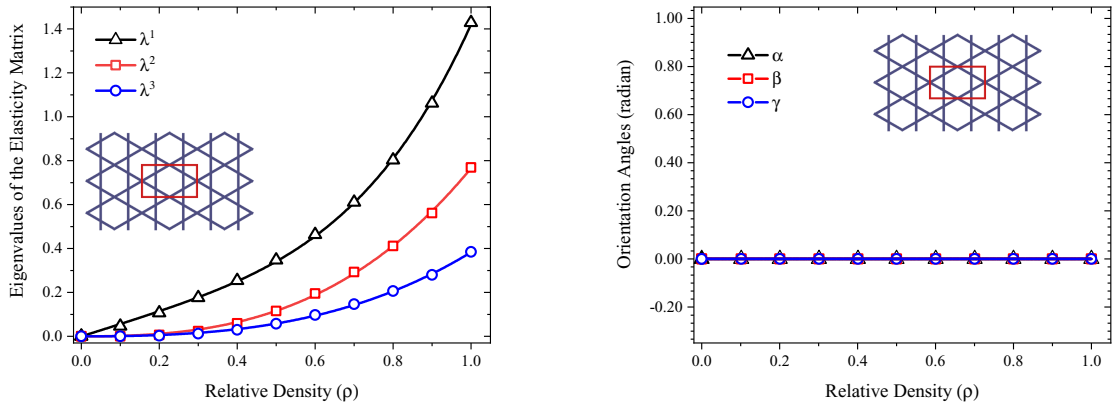

(a) (b)

Figure 8: Fitting curves for (a) eigenvalues, and (b) orientation angle of eigenvectors, for a Kagome microstructure.

5.2. Orthogonal-isotropic cross-shaped microstructure

For the orthogonal-isotropic cross-shaped microstructure, three independent eigenvalue fitting functions are needed, while the orientation angles remain unchanged as established in Appendix A; see Fig. 9. This

is consistent with the 3 independent constants in the corresponding $\boldsymbol{C}$ matrix.

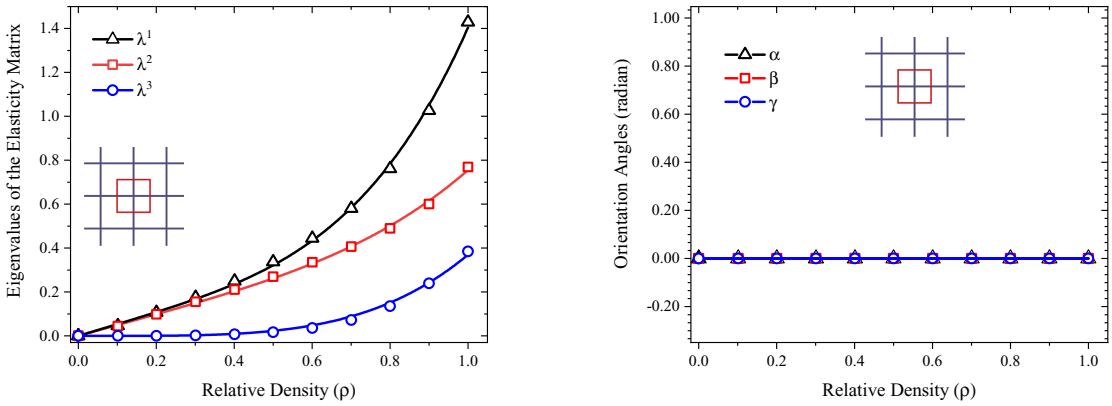

(a) (b)

Figure 9: Fitting curves for (a) eigenvalues, and (b) orientation angle of eigenvectors, for a Cross microstructure.

5.3. Orthotropic mixed-triangular microstructure

For the orthotropic mixed-triangular microstructure, three distinct eigenvalue fitting functions, and one angle fitting function are needed as observed from Fig. 10. This is consistent with the 4 independent constants in the corresponding $\boldsymbol{C}$ matrix.

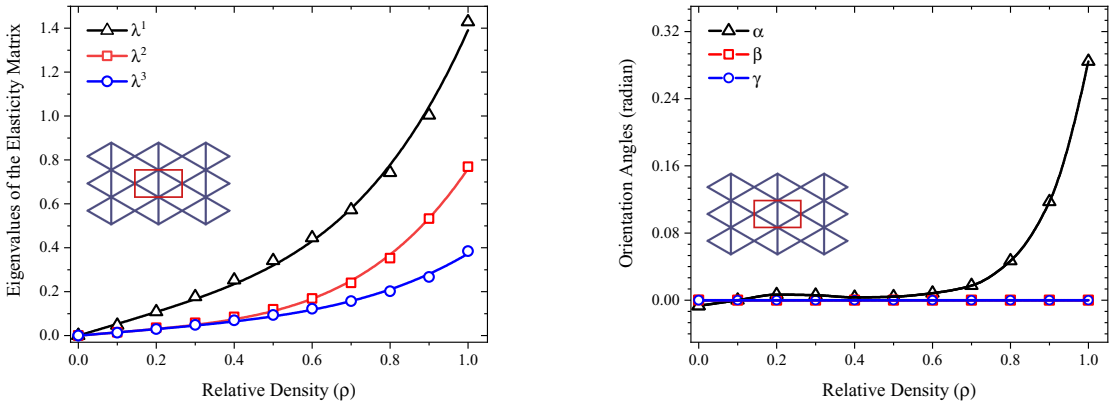

(a) (b)

Figure 10: Fitting curves for (a) eigenvalues, and (b) orientation angle of eigenvectors, for a mixed-triangular microstructure.

5.4. General anisotropic Z-shaped microstructure

Finally, for the general anisotropic Z-shaped microstructure, six fitting functions are required to interpolate the effective elasticity matrix as in Fig. 11. This is consistent with the 6 independent constants in the corresponding $\boldsymbol{C}$ matrix.

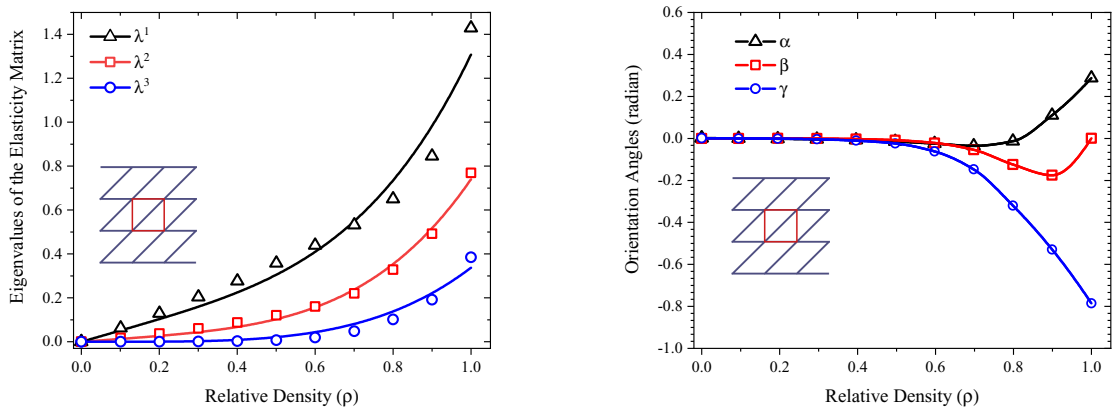

(a) (b)

Figure 11: Fitting curves for (a) eigenvalues, and (b) orientation angle of eigenvectors, for a Z microstructure.

5.5. Summary for 2D microstructures

The above observations are summarized in the Table 1.

Table 1: Curve fitting based on spectral decomposition for various 2D symmetry types (groups).

	(a)	(b)	(c)	(d)
Topology	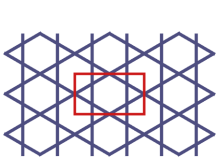	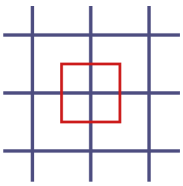	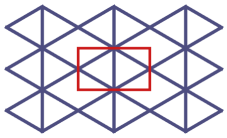	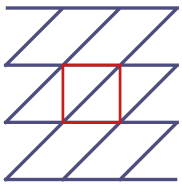
Symmetry type	Isotropic	Orthogonal-isotropic	Orthotropic	General anisotropic
Elasticity matrix constants	$\begin{bmatrix} \blacksquare & \blacklozenge & 0 \\ & \blacksquare & 0 \\ & & (\blacksquare - \blacklozenge)/2 \end{bmatrix}$	$\begin{bmatrix} \blacksquare & \blacklozenge & 0 \\ & \blacksquare & 0 \\ & & \bullet \end{bmatrix}$	$\begin{bmatrix} \blacksquare & \blacklozenge & 0 \\ & \blacktriangle & 0 \\ & & \bullet \end{bmatrix}$	$\begin{bmatrix} \blacksquare & \blacklozenge & \bigstar \\ & \blacktriangle & \blacktriangledown \\ & & \bullet \end{bmatrix}$
Number of distinct eigenvalues	2	3	3	3
Number of orientation angles	0	0	1	3
Number of independent fitting functions	2	3	4	6

Number of different symbols in 'Elasticity matrix constants' row represent independent terms.

5.6. Extension to 3D

While the focus of this work is on 2D microstructures, the spectral decomposition method can be extended to 3D. Similar to 2D classification, 3D microstructures can be categorized based on material symmetry, such as cubic, transversely isotropic, orthotropic, monoclinic and triclinic [78]. For example, consider the cubic microstructure in Fig. 12a. It has three mutually orthogonal planes of reflection symmetry, and 90° rotation symmetry with respect to those planes. Hence, the number of independent constants required to describe this microstructure is three. Through spectral decomposition of the [6 × 6] elasticity matrix, we obtain three unique eigenvalues, whose regression is illustrated in Fig. 12b.The eigenvector matrix remains constant, and does not require interpolation.

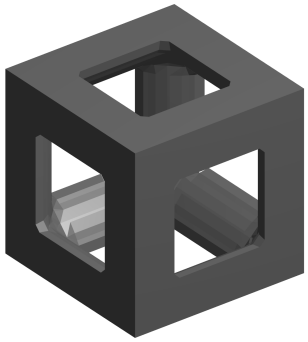

(a)

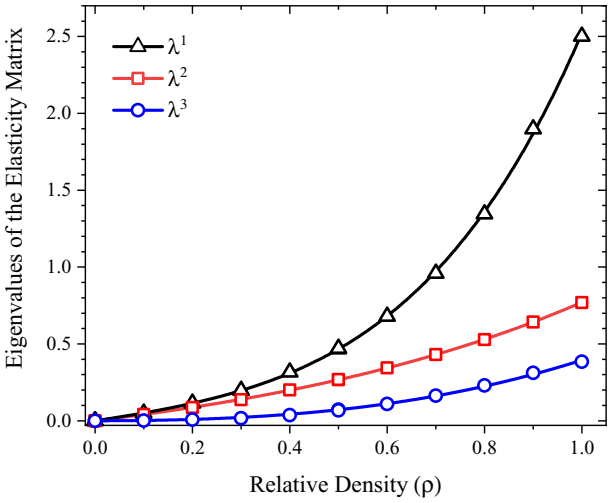

(b)

Figure 12: (a) A 3D cubic microstructure, and (b) its fitting curves for eigenvalues.

On the other hand, consider a triclinic microstructure [78]. These have no symmetry planes, and are fully anisotropic: the number of independent coefficients required to construct the elasticity matrix is 21. Consequently, we must interpolate 6 eigenvalues and 15 orientation angles, i.e., 21 fitting functions will be needed. The implementation of 3D spectral decomposition will be pursued in the future.

6. Template Stiffness Matrices

Observe that, in the current framework, every macro-element has a corresponding elasticity matrix $\boldsymbol{C}_{\mathrm{EL}}$, depending on its density ρ_{EL}, at that instance. This entails computing the stiffness matrix $\boldsymbol{K}^{\mathrm{E}}$ for every $\boldsymbol{C}_{\mathrm{EL}}$ i.e. $\boldsymbol{K}^{\mathrm{E}}(\boldsymbol{C}_{\mathrm{EL}})$ via numerical integration, for each iteration of the optimization process. This can be computationally expensive. We propose here to use the concept of template stiffness matrices [79, 22] for computational efficiency.

The key concept is to construct, prior to optimization, *unit* elasticity matrices, $\boldsymbol{C}^{(i)}$ using the three dimensional unit vectors $\boldsymbol{e}_i$ as follows:

$$\boldsymbol{C}^{(i)} = \boldsymbol{e}_i \otimes \boldsymbol{e}_i \qquad i = 1,2,3 \quad \text{(no summation over } i\text{)} \tag{16}$$

$$\boldsymbol{C}^{(i+j+1)} = \boldsymbol{e}_i \otimes \boldsymbol{e}_j + \boldsymbol{e}_j \otimes \boldsymbol{e}_i \qquad i = 1,2;\ i < j \leq 3 \tag{17}$$

where the first three indices correspond to the three diagonal components of elasticity matrix and last three correspond to off-diagonal components. Then, the corresponding *unit* stiffness matrices are computed (again, prior to optimization) via

$$\boldsymbol{K}^{(i)} = \boldsymbol{K}^{\mathrm{E}}\left(\boldsymbol{C}^{(i)}\right) \qquad i = 1,2,\ldots,6 \tag{18}$$

Then, during optimization, given any matrix $\boldsymbol{C}_{\mathrm{EL}}$, the element stiffness matrix can be easily computed via

$$\boldsymbol{K}^{\mathrm{E}}(\boldsymbol{C}_{\mathrm{EL}}) = C_{11}(\rho)\boldsymbol{K}^{(1)} + C_{22}(\rho)\boldsymbol{K}^{(2)} + C_{33}(\rho)\boldsymbol{K}^{(3)} + C_{12}(\rho)\boldsymbol{K}^{(4)} + C_{13}(\rho)\boldsymbol{K}^{(5)} + C_{23}(\rho)\boldsymbol{K}^{(6)} \tag{19}$$

where $C_{ij}(\rho)$ is the (i,j) component of $\boldsymbol{C}_{\mathrm{EL}}$ at $\rho = \rho_{\mathrm{EL}}$. This reduces the computation significantly as the numerical experiments indicate. Further improvements can be made based on the observation made regarding elasticity matrix symmetry group in the previous section.

For isotropic and orthogonal-isotropic elasticity matrices, the eigenvectors do not vary with the density. For these microstructures, the elasticity matrix for an element EL is dependent only on the relative density through the three eigenvalues:

$$\boldsymbol{C}_{\mathrm{EL}} = \sum_{i=1}^{3} q^{(i)}(\rho_{\mathrm{EL}}) \left(\boldsymbol{v}^{(i)} \otimes \boldsymbol{v}^{(i)}\right) \tag{20}$$

where $\boldsymbol{v}^{(1,2,3)}$ are the three constant eigenvectors given in Appendix A and $q^{(i)}(\rho_{\mathrm{EL}})$ is the value of i^{th} eigenvalue polynomial regression function evaluated at ρ_{EL}. Thus, the number of templates can be reduced from six to three. These templates are computed as:

$$\boldsymbol{K}^{(i)}_{\mathrm{red}} = \boldsymbol{K}^{\mathrm{E}}\left(\boldsymbol{v}^{(i)} \otimes \boldsymbol{v}^{(i)}\right) \qquad i = 1,2,3 \tag{21}$$

Then, the element stiffness matrix for any element EL is computed as

$$\boldsymbol{K}^{\mathrm{E}}(\boldsymbol{C}_{\mathrm{EL}}) = \sum_{i=1}^{3} q^{(i)}(\rho_{\mathrm{EL}})\boldsymbol{K}^{(i)}_{\mathrm{red}} \tag{22}$$

Further, as shown in Appendix B, the third eigenvalue is always half of either of the other two. Therefore for isotropic microstructures, the third eigenvalue fitting function $q^{(3)}$ can be expressed as the linear combination of the other two using scalars a_1 and a_2:

$$q^{(3)}(\rho) = a_1 q^{(1)}(\rho) + a_2 q^{(2)}(\rho) \tag{23}$$

$$\implies \boldsymbol{K}^{\mathrm{E}}(\boldsymbol{C}_{\mathrm{EL}}) = \sum_{i=1}^{2} q^{(i)}(\rho_{\mathrm{EL}}) \left(\boldsymbol{K}^{(i)}_{\mathrm{red}} + a_i \boldsymbol{K}^{(3)}_{\mathrm{red}}\right)$$

$$\implies \boldsymbol{K}^{\mathrm{E}}(\boldsymbol{C}_{\mathrm{EL}}) = \sum_{i=1}^{2} q^{(i)}(\rho_{\mathrm{EL}})\boldsymbol{K}^{(i)}_{\mathrm{iso}} \tag{24}$$

where

$$\boldsymbol{K}^{(i)}_{\mathrm{iso}} = \boldsymbol{K}^{(i)}_{\mathrm{red}} + a_i \boldsymbol{K}^{(3)}_{\mathrm{red}} \qquad i = 1,2 \tag{25}$$

are the two element stiffness matrix templates required for isotropic microstructures. Note that the scalars $\{a_1, a_2\}$ are either $\{0.5, 0\}$ or $\{0, 0.5\}$. The computational benefits of these templates are discussed under numerical experiments.

7. Sensitivity analysis

Here, we consider sensitivity analysis that is essential during optimization. Recall that the compliance is defined as

$$J = \sum_{\mathrm{EL}} \boldsymbol{u}^{\mathsf{T}}_{\mathrm{EL}} \boldsymbol{K}^{\mathrm{E}}(\boldsymbol{C}_{\mathrm{EL}}) \boldsymbol{u}_{\mathrm{EL}} \tag{26}$$

The sensitivity of the compliance with respect to the design variables is computed as

$$\frac{\partial J}{\partial \rho_{\mathrm{EL}}} = -\boldsymbol{u}_{\mathrm{EL}}^{\mathsf{T}} \boldsymbol{K}^{\mathrm{E}} \left(\frac{\partial \boldsymbol{C}_{\mathrm{EL}}}{\partial \rho_{\mathrm{EL}}} \right) \boldsymbol{u}_{\mathrm{EL}} \tag{27}$$

where using Eqn. 8

$$\frac{\partial \boldsymbol{C}_{\mathrm{EL}}}{\partial \rho_{\mathrm{EL}}} = \left(\frac{\partial \boldsymbol{V}(\rho)}{\partial \rho} \boldsymbol{\Lambda}(\rho) \boldsymbol{V}^{\mathsf{T}}(\rho) + \boldsymbol{V}(\rho) \frac{\partial \boldsymbol{\Lambda}(\rho)}{\partial \rho} \boldsymbol{V}^{\mathsf{T}}(\rho) + \boldsymbol{V}(\rho) \boldsymbol{\Lambda}(\rho) \frac{\partial \boldsymbol{V}^{\mathsf{T}}(\rho)}{\partial \rho} \right)_{\rho=\rho_{\mathrm{EL}}} \tag{28}$$

Exploiting Eqn. 7

$$\left. \frac{\partial \boldsymbol{V}(\rho)}{\partial \rho} \right|_{\rho=\rho_{\mathrm{EL}}} = \left. \frac{\partial \boldsymbol{R}(r(\rho), s(\rho), t(\rho))}{\partial \rho} \right|_{\rho=\rho_{\mathrm{EL}}} \boldsymbol{B}_{\mathrm{R}} \tag{29}$$

and Eqn. 4

$$\left. \frac{\partial \boldsymbol{\Lambda}_{ii}(\rho)}{\partial \rho} \right|_{\rho=\rho_{\mathrm{EL}}} = \left. \frac{\mathrm{d}q^{(i)}(\rho)}{\mathrm{d}\rho} \right|_{\rho=\rho_{\mathrm{EL}}} \qquad i = 1, 2, 3 \tag{30}$$

Again, using Eqn. 7

$$\begin{aligned} \left. \frac{\partial \boldsymbol{R}(r(\rho), s(\rho), t(\rho))}{\partial \rho} \right|_{\rho=\rho_{\mathrm{EL}}} = \Bigg(& \frac{\partial \boldsymbol{R}_z(r(\rho))}{\partial \rho} \boldsymbol{R}_y(s(\rho)) \boldsymbol{R}_x(t(\rho)) \\ & + \boldsymbol{R}_z(r(\rho)) \frac{\partial \boldsymbol{R}_y(s(\rho))}{\partial \rho} \boldsymbol{R}_x(t(\rho)) \\ & + \boldsymbol{R}_z(r(\rho)) \boldsymbol{R}_y(s(\rho)) \frac{\partial \boldsymbol{R}_x(t(\rho))}{\partial \rho} \Bigg) \Bigg|_{\rho=\rho_{\mathrm{EL}}} \end{aligned} \tag{31}$$

and using Eqn. 13

$$\left. \frac{\mathrm{d}q^{(i)}(\rho)}{\mathrm{d}\rho} \right|_{\rho=\rho_{\mathrm{EL}}} = \sum_{j=1}^{d} j q_j^{(i)} \rho^{j-1} \qquad i = 1, 2, 3 \tag{32}$$

The derivatives in Eqn. 31 can be derived using the expressions for rotation matrix and eqn. 15.

In Eqn. 28, even though the second term is positive definite, the first and third terms together are symmetric but not necessarily positive definite. This implies that the derivative of interpolated effective elasticity matrix in Eqn. 28 may not be positive definite even when the interpolated effective elasticity matrix itself is positive definite. Thus, the sensitivity of objective function in Eqn. 27 might change sign. However, the sensitivity terms can be offset by the highest positive value to ensure all sensitivity terms are non-positive during the design update using optimality criteria [80, 81]. In the special case of constant eigenvectors, i.e., when the orientation angles do not vary with relative density, the first and third term in Eqn. 28 vanish, and this problem does not arise.

8. Algorithm

In summary, the proposed graded multi-scale optimization procedure is captured in Algorithm 2; the design variables are the density values ρ_{EL} over each macro-element.

For comparison, the (classic) direct method is captured in Algorithm 3. Observe that the main differences between the two algorithms is in step 4: computing $\boldsymbol{C}_{\mathrm{EL}}$, and step 5: computing $\boldsymbol{K}_{\mathrm{EL}}$.

Algorithm 2 Graded MTO: Proposed Spectral Decomposition (SD) Method

1: Initialize
   a: Set analysis and optimization parameters
   b: Initialize design variables ρ_{EL} for all macro-elements EL
   c: Precompute template stiffness matrices ▷ using Eqn. 18,21, or 25
2: **while** Not Converged **do**
3: **for** each ρ_{EL} **do**
4: Compute $\boldsymbol{C}_{\mathrm{EL}}$
      a: Find the 3 eigenvalues and 3 orientation angles ▷ using Eqn. 13 and 15
      b: Compute the elasticity matrix $\boldsymbol{C}_{\mathrm{EL}}$ ▷ using eqn. 8
5: Compute element stiffness matrices $\boldsymbol{K}^{\mathrm{E}}(\boldsymbol{C}_{\mathrm{EL}})$ ▷ using eq 19, 22, or 24
6: **end for**
7: Solve and update design variables
   a: Assemble stiffness matrix and solve eq. (1b) or use matrix-free techniques [82, 83]
   b: Compute sensitivity of objective and constraint ▷ see section 7
   c: Update the design variables ρ_{EL} using optimality criteria method
8: **end while**

Algorithm 3 Graded MTO: Direct Method

1: Same as algorithm 2 ▷ using Eqn. 18
2: **while** Not Converged **do**
3: **for** each ρ_{EL} **do**
4: Compute independent $\boldsymbol{C}_{\mathrm{EL}}$ components via direct regression
5: Compute element stiffness matrices $\boldsymbol{K}^{\mathrm{E}}(\boldsymbol{C}_{\mathrm{EL}})$ ▷ using eq 19
6: **end for**
7: Same as algorithm 2 ▷ using Eqn. 27
8: **end while**

9. Numerical Experiments

In this section, we will conduct several numerical experiments, addressing the following topics.

- **Robustness:** We compare the robustness of the direct and proposed method of interpolation, by comparing the strain energies for a sample problem at various density values.
- **Accuracy:** Next, we compare the interpolation accuracy of the two methods,
- **Graded MTO:** We then focus on graded multi-scale optimization, and explore the following topics:
  1. **Sensitivity to microstructure type:** Here we consider the impact of the microstructure on the computed topology.

2. **Sensitivity to degree of regression:** Next, the impact of degree of regression on the computed topology is considered via the proposed method.
3. **Designs at low volume fractions:** Here, we explore designs at low volume fractions, and provide interpretations to the topologies.
4. **Computation time:** Finally, we compare the computational times of the two methods.

The default values for the simulation parameters are as follows:

- Base material is isotropic with Poisson's ratio of 0.3 and unit Young's modulus.
- The degree of eigenvalue polynomial regression is four (unless stated otherwise). Cubic spline interpolation is used for orientation angles.
- In the asymptotic homogenization implementation, the 2-D microstructure domain is discretized into 10000η bilinear quadrilateral micro-elements, where η is the aspect ratio of the microstructure domain. Note that the Kagome and mixed-triangular microstructure are of aspect ration $\sqrt{3}:1$ whereas the cross and Z-shaped microstructures have an aspect ratio of 1:1.
- The target volume fraction is 50%, unless otherwise stated.
- A sensitivity filter of radius 1.2×the mean size of an element is used.
- An optimality criteria update with an exact Lagrange multiplier computation [84] is used.
- The implementation is in MATLAB R2020a, on a standard Windows 10 desktop with Intel(R) Core(TM) i7-4790 CPU running at 3.6 GHz with 32 GB memory.
- The optimization terminates when (1) the maximum change among the design variables is below 0.001, or (2) the relative change in objective function drops below 1×10^{-6} for two consecutive iterations, or (3) the number of iterations reaches a maximum value of 800.

9.1. Robustness

Recall from Section 2 that the direct method may lead to non-positive definite elasticity matrices, which translates into a negative strain energy estimate. To illustrate this, we consider the mid-edge loaded cantilever illustrated in Fig. 13. The domain is discretized into 100×50 elements. Then, for various density values ranging from $\rho_{\min}$ to 1, the cross-shaped microstructure is constructed (see Fig. 6) over all elements. Then the corresponding element stiffness matrices are computed using (a) the direct method, and (b) the proposed spectral decomposition method. Then, the two resulting finite element problems are solved, and the strain energies computed.

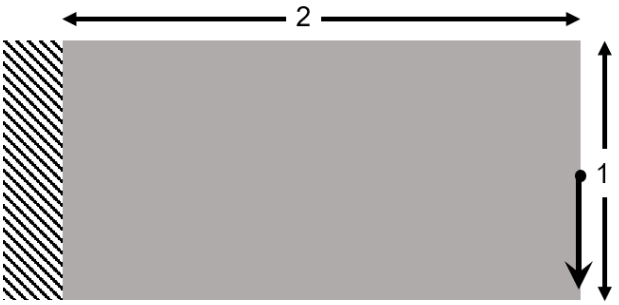

Figure 13: Cantilever design domain subject to graded MTO.

Fig. 14 illustrates the strain energy computed using the direct method as a function of the density, for various degrees of interpolation. Observe that, for degree-5 and degree-6, the strain energy becomes negative (discontinuity in the logarithmic scale) for certain intermediate density values. Further, for degree-4, and for this particular choice of microstructure and design domain, the strain energy remains positive. The main conclusion is that one cannot guarantee the positive definiteness in the direct method.

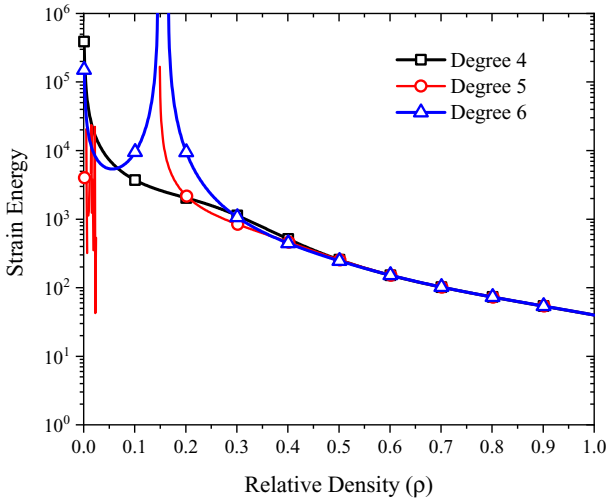

Figure 14: Strain energy computed using the direct method.

On the other hand, Fig. 15 illustrates the strain energy computed via the proposed spectral decomposition methods. The strain energy remains positive for all values of ρ, as expected.

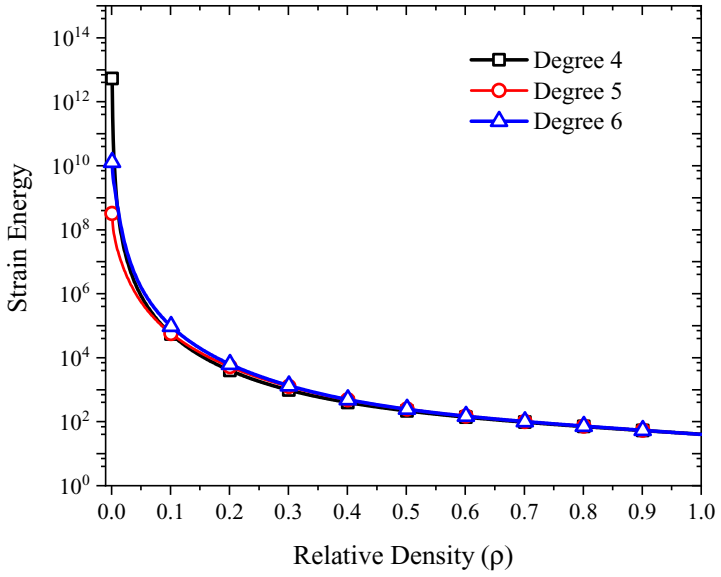

Figure 15: Strain energy computed using the spectral decomposition method.

9.2. Accuracy

Next we compare the accuracy of the two methods. Since the eigenvalue polynomials are required to be positive in the proposed method (i.e., an additional constraint), we expect it to be less accurate than the direct method. The accuracy of the two methods are compared for the four different microstructures discussed earlier, using the popular R^2 metric. We consider 50 instances of the densities at which we first compute the 'exact' elasticity matrix $\boldsymbol{C}^{\mathrm{AH}}$, using AH. Then, for the same density values, the elasticity matrices are computed using the direct and proposed spectral decomposition (SD) method of interpolation, using 10 samples in each case for interpolation (see Algorithm 2 and Algorithm 3). Then the R^2 metric is computed as for each component as follows:

$$R^2_{ij} = 1 - \frac{\sum_{l=1}^{50} \left(C^{\mathrm{AH}}_{ij}(\rho_l) - C_{ij}(\rho_l)\right)^2}{\sum_{l=1}^{50} \left(C^{\mathrm{AH}}_{ij}(\rho_l) - \overline{C}^{\mathrm{AH}}_{ij}\right)^2} \tag{33}$$

where $\overline{C}^{\mathrm{AH}}_{ij}$ is the mean C^{AH}_{ij} over 50 instances. Note that closer the value of R^2 to unity, the better is the fit.

For the four microstructure, the R^2 values are illustrated in Fig. 16 by solid and dashed curves for the proposed and direct methods, respectively. Only a few components are illustrated for clarity; all other components exhibit similar behavior.

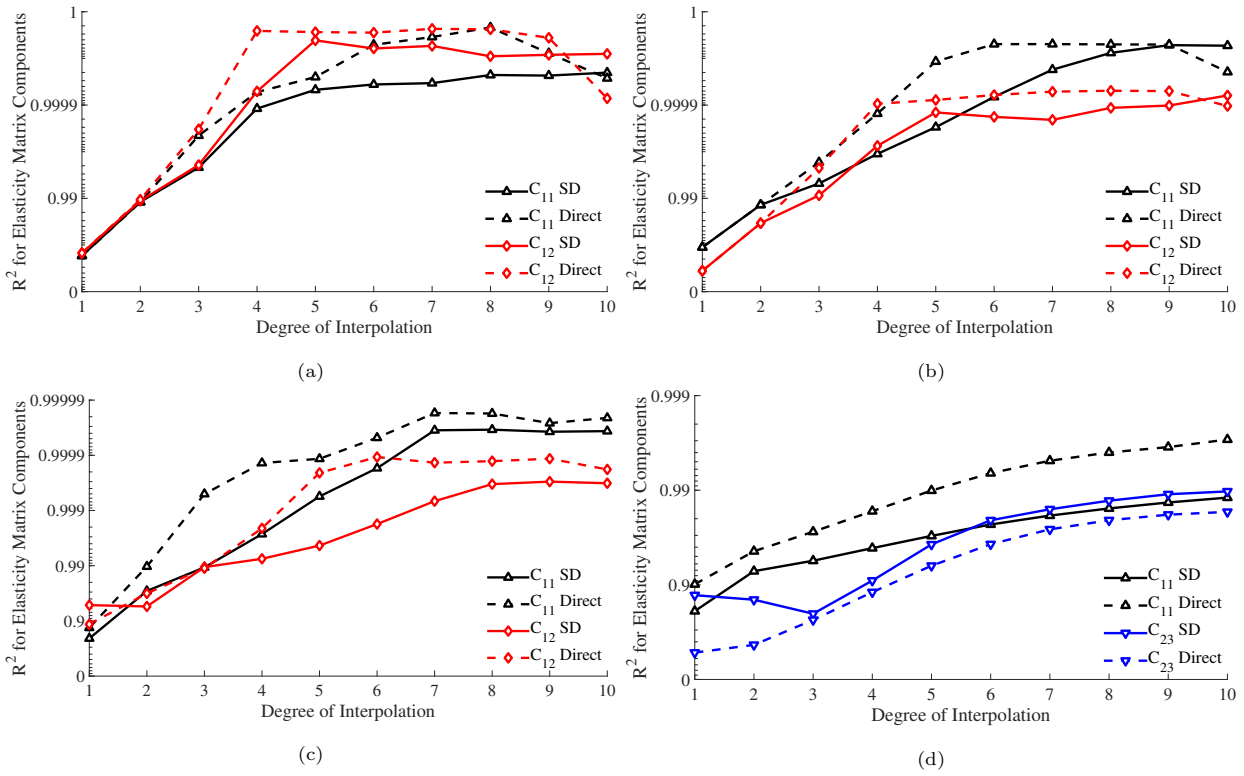

Figure 16: R^2 of proposed method and direct polynomial regression of some elasticity matrix components for (a) Kagome, (b) Cross, (c) Mixed-triangular, and (d) Z-shaped graded-microstructures.

The key observation from these plots is that the direct method is slightly more accurate (but not always) than the SD method. However, the possible increase in accuracy of the direct method is overshadowed by its lack of robustness, as discussed in the previous experiment.

9.3. Graded MTO

We now illustrate the proposed SD method for graded multi-scale topology optimization.

9.3.1. Impact of Microstructure Type

In this first experiment of graded MTO, the cantilever domain illustrated in Fig. 13 is optimized using the four microstructures described earlier. The design domain is discretized using congruent elements of aspect ratio η, corresponding to that of the microstructure, resulting in mesh of sizes 100×50 for the cross and Z-shaped microstructures, and 76 $\times66$, for the Kagome and mixed-triangular microstructures.

The resulting topologies along with the compliance values are illustrated in Fig. 17. Observe the asymmetry in the design for the asymmetric Z microstructure. The Z-shaped microstructure takes the longest to converge.

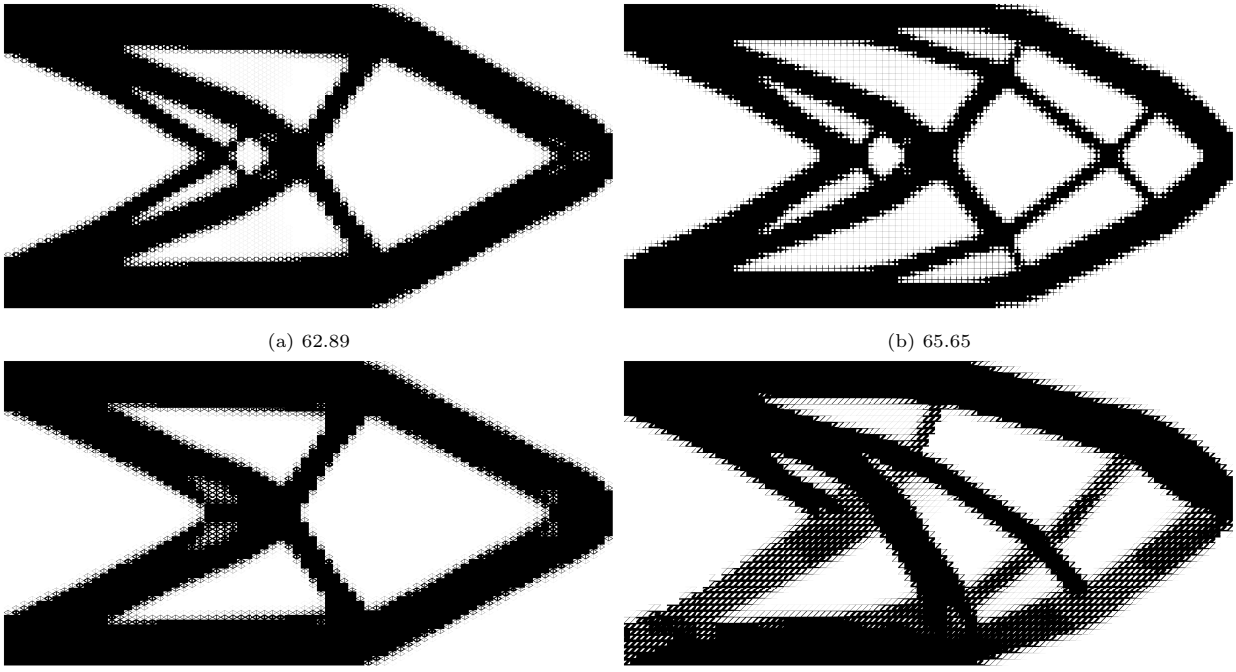

(a) 62.89 (b) 65.65

(c) 63.78 (d) 70.00

Figure 17: Graded MTO designs for microstructures: (a) Kagome, (b) Cross, (c) Mixed-triangular, and (d) Z-shaped.

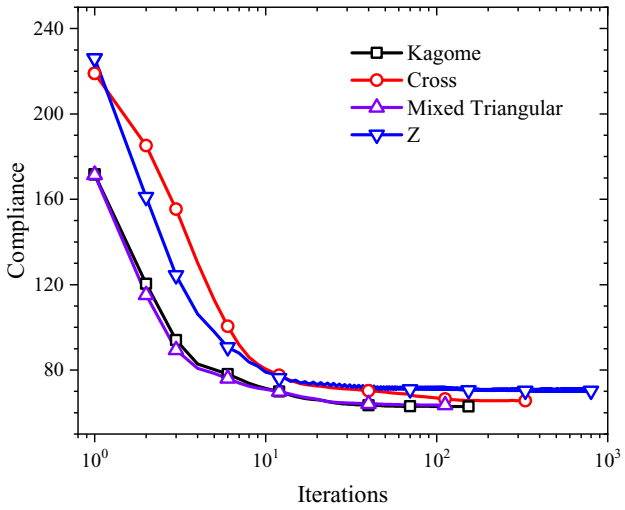

Figure 18: Convergence history for the four microstructure types, for a cantilever design domain.

9.3.2. Impact of Degree of Fit

Next, the impact of degree of eigenvalue fitting function on graded MTO design is studied on a half MBB beam in Fig. 19. (The angle interpolation via cubic splines remains unchanged in all the experiments.) As in the previous experiment, the domain is discretized with 100×50 elements for the cross and Z-shaped microstructures, and 76×66 elements, for the Kagome and mixed-triangular microstructures.

Figure 19: MBB beam design domain for graded MTO.

The topologies for degree 4, 5 and 6, using the four microstructures are illustrated in Fig. 20, together with the final compliance values. The important conclusions are: (1) the compliance is almost a constant for the first two microstructures since the improvement in R^2 metric from degree to 4 to degree 6 is small (1×10^{-4}), whereas the compliance decreases for the other two microstructures since the R^2 metric improvement is significant (1×10^{-2}), and (2) for the same reason, the change in topology is minimal for Kagome, Cross, and mixed-triangular, whereas for the Z-shaped microstructure, the change in topology is significant.

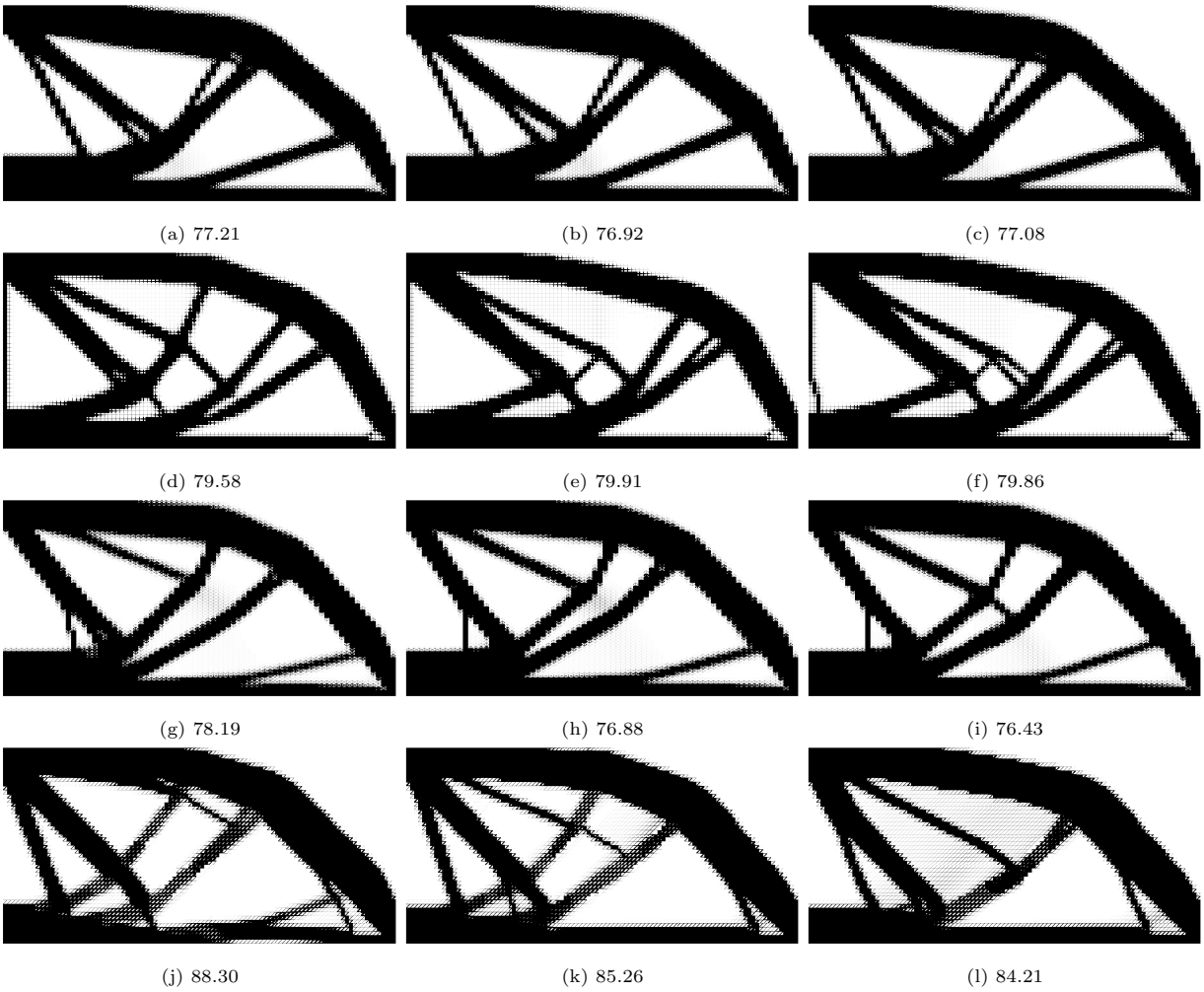

(a) 77.21 (b) 76.92 (c) 77.08

(d) 79.58 (e) 79.91 (f) 79.86

(g) 78.19 (h) 76.88 (i) 76.43

(j) 88.30 (k) 85.26 (l) 84.21

Figure 20: Graded MTO designs using eigenvalue fitting functions of degree 4, 5, and 6 (from left to right) for Kagome, Cross, Mixed-triangular, and Z-shaped (from top to bottom) microstructures

9.3.3. Designs of Low Volume Fractions

Next, an L-bracket with unit point load illustrated earlier in Fig. 1 is considered for this experiment. An orthogonal-isotropic X-shaped microstructure is used here, and the domain is discretized into 6400 elements. Graded MTO designs at multiple volume fractions are generated using degree-4 eigenvalue fitting functions.

The designs and their compliances are illustrated in Fig. 21. Observe that all designs exhibit large areas of partial fills. This is a unique characteristic of the X-shaped microstructure for reasons explained below.

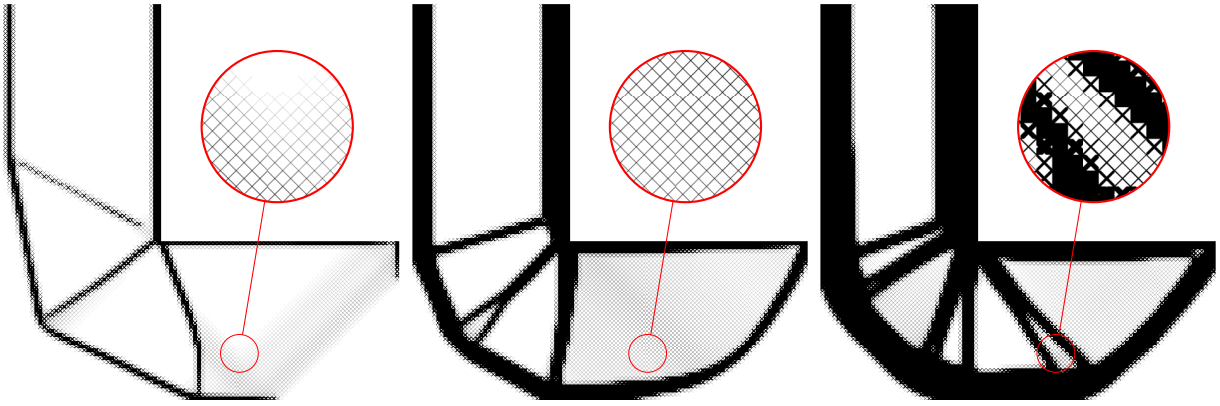

(a) 1130.66 (b) 283.97 (c) 179.61

Figure 21: Graded MTO designs using SD method with degree-4 fitting functions for volume constraint of 10%, 30%, and 50% (from left to right) for X-shaped microstructure. Inset shows graded-microstructure at the same region of design domain.

Observe in Fig. 22 that all components of the elasticity matrix vary almost linearly with density, when density is below 0.25. In other words, there is no penalization for low density values. This is similar to SIMP with $p = 1$ where the Young's modulus is linearly dependent on the density, resulting in large partial density regions.

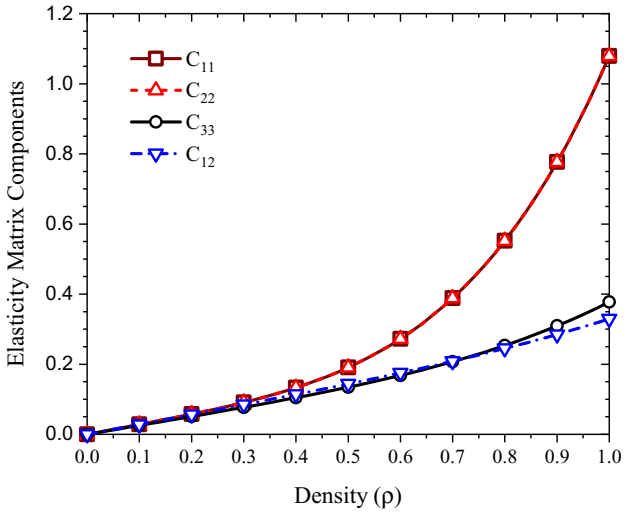

Figure 22: Elasticity matrix fitting functions obtained for degree 4 eigenvalue curves for X-shaped microstructures. Curves for C_{11} and C_{22} coincide.

9.3.4. Computational Costs

Finally, we compare the computational times for the two methods (direct vs. proposed), with and without the use of templates (see section 6). The cantilever beam in Fig. 13 is again chosen for this experiment. As delineated in Algorithms 2 and 3, the two methods only differ in steps 4 and 5, i.e., in the computation of $\boldsymbol{C}_{\mathrm{EL}}$ and $\boldsymbol{K}^{\mathrm{E}}(\boldsymbol{C}_{\mathrm{EL}})$. The computational times for these two steps are summarized in Table 2 and Table 3,

respectively.

The main conclusions from Table 2 are that: (1) templates have no impact on the direct method for computing $\boldsymbol{C}_{\mathrm{EL}}$, but they significantly accelerate the SD method for the isotropic and orthogonal-isotropic structures, and (2) the direct method is faster than the proposed method for the orthotropic and anisotropic structures. The reason for these observations is that the SD method for orthotropic and anisotropic structures requires expensive matrix multiplications associated with Eqn. 8. Direct method, in contrast to SD, requires few polynomial function evaluations without the expensive matrix multiplications. With maximum six function evaluations, direct method thus takes lesser time compared to SD method for these structures. On the other hand, for the structures of isotropic and orthogonal-isotropic type, both the methods require polynomial evaluations without matrix multiplications. Moreover, fewer templates and function evaluations are required for SD method compared to direct method. Use of templates reduces the number of computations for SD method, thus reducing the computation time for $\boldsymbol{C}_{\mathrm{EL}}$.

Table 2: Computation time (in seconds) for elasticity matrix $\boldsymbol{C}_{\mathrm{EL}}$ during the first 100 iterations

	Method	Kagome (isotropic)	Cross (orthogonal-isotropic)	Mixed-Triangular (orthotropic)	Z (anisotropic)
Without Template	Direct Regression	0.04	0.04	0.04	0.10
	Proposed SD	0.24	0.36	0.93	0.90
With Template	Direct Regression	0.04	0.04	0.04	0.10
	Proposed SD	0.02	0.02	0.89	0.88

On the other hand, the main conclusions from Table 3 are: (1) templates have a major impact on both methods for computing $\boldsymbol{K}^{\mathrm{E}}(\boldsymbol{C}_{\mathrm{EL}})$, (2) the SD method is marginally superior in cost for the first two types of microstructures, while both methods are comparable in cost for the other two microstructures.

Table 3: Computation time (in seconds) for element stiffness matrix $\boldsymbol{K}^{\mathrm{E}}(\boldsymbol{C}_{\mathrm{EL}})$ during the first 100 iterations

	Method	Kagome (isotropic)	Cross (orthogonal-isotropic)	Mixed-Triangular (orthotropic)	Z (anisotropic)
Without Template	Direct Regression	9.65	9.79	9.71	9.66
	Proposed SD	9.63	9.67	9.72	9.69
With Template	Direct Regression	0.42	0.42	0.42	0.56
	Proposed SD	0.27	0.35	0.39	0.53

Thus, in summary, (1) the use of templates is highly recommended, independent of the method used,

and (2) the direct method is computationally superior to the SD method for orthotropic and anisotropic microstructures.

9.3.5. Graded MTO: Direct versus SD

The importance of positive-definiteness during MTO is illustrated in this subsection. We consider the cantilever design domain in Fig. 13 with the Z-shaped graded microstructure. Fig. 23 illustrates the components of the $\boldsymbol{C}$ matrix obtained by the direct method, and the SD method. The blue bar on top indicates the densities for which the $\boldsymbol{C}$ matrix remains positive-definite. For the SD method, the $\boldsymbol{C}$ matrix is always positive definite. Note that C_{13} and C_{23} become negative in the SD method when the density is close to 1, yet $\boldsymbol{C}$ remains positive definite. On the other hand, for the direct method, for densities less then 0.1 and around 0.4, positive-definiteness is lost. The strain energy of the corresponding elements becomes negative, translating into an erroneous drop/fluctuation in compliance as can be observed in Fig. 24. These fluctuations affect the stability of the optimization algorithm. The total strain energy can also become negative if large number of elements lose positive definiteness. Finally, the resulting topologies are illustrated in Fig. 25, where one can observe that the direct method has failed to converge to a well-defined topology.

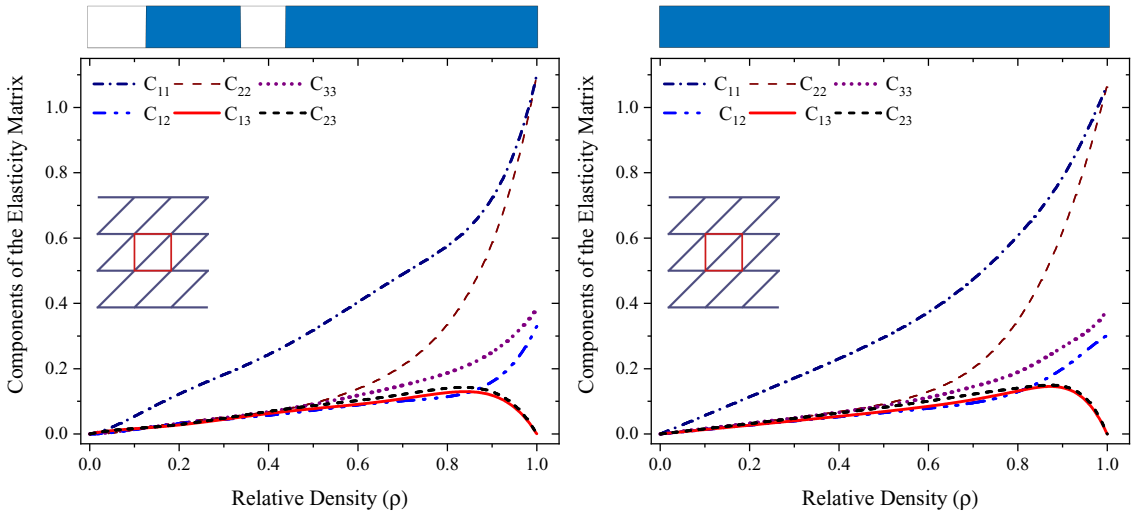

Figure 23: Components of the $\boldsymbol{C}$ matrix for a Z-shaped graded microstructure using (a) direct and (b) SD methods. Blue bars (on top) show the region of positive definite $\boldsymbol{C}$.

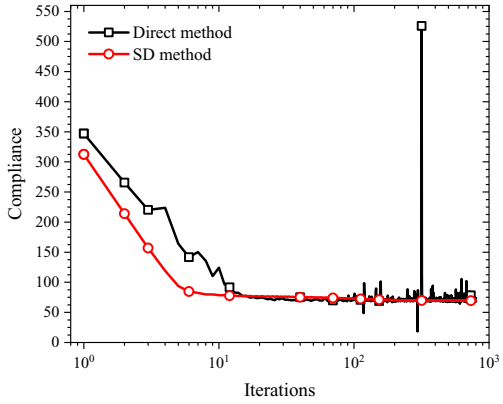

Figure 24: Convergence plot for direct method and SD method

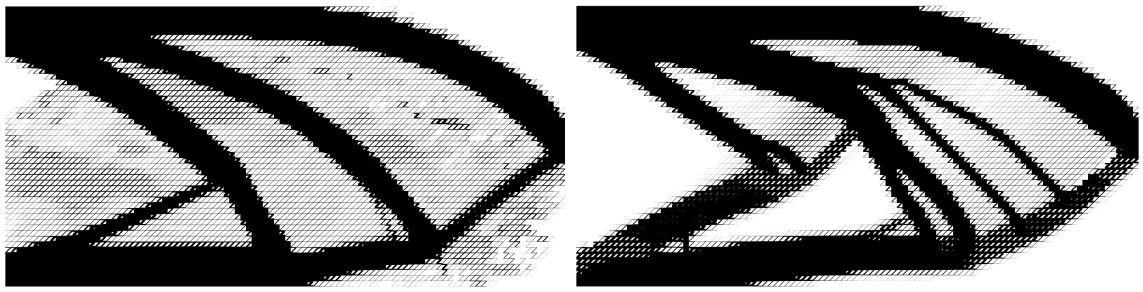

(a) (b)

Figure 25: Graded MTO designs using Z-shaped graded microstructure. (a) Direct method and (b) SD method

10. Conclusions

In this paper, we demonstrated spectral decomposition (SD) method for generating positive-definite elasticity matrices of graded-microstructures. This is achieved by constraining the polynomial-based regression of eigenvalues to be positive.

The SD method is shown to be robust and sufficiently accurate for all symmetry types including isotropic, orthogonal-isotropic, orthotropic and anisotropic graded-microstructures. Several numerical experiments are conducted to characterize the proposed method and its application to MTO. The most important conclusion from the first experiment is that, unlike the SD method, one cannot always rely on the direct method to converge. For the SD method, it was also observed that the degree of polynomial regression for eigenvalues increases the accuracy. This can alter the topology, and in some cases significantly improve the compliance. The computational cost of the SD method is lower than the direct method for isotropic and orthogonal-isotropic microstructures. The use of matrix templates was shown to reduce computational cost for both direct and SD methods. The SD method ensures positive definiteness and monotonicity of $\boldsymbol{C}$ matrix components for isotropic and orthogonal-isotropic graded-microstructures. However, for orthotropic and anisotropic microstructures, while positive-definiteness is ensured by the SD method, the monotonicity is influenced by

the instances selected for AH and the subsequent use of spline-interpolation.

The limitations of the SD method are: (1) the computational cost is higher for orthotropic and anisotropic microstructures, (2) the derivative of the interpolated elasticity matrix may not be positive definite, and (3) due to the non-monotonic behavior of the orientation angles, spline interpolation, rather than the simpler polynomial interpolation must be used.

There are several related topics that need to be explored. Extension of the SD method to 3-D and curved microstructure can be explored. Further, we assumed in this paper that the orientation of the microstructures does not vary spatially. A coupled orientation and density optimization may lead to better designs [22, 79]. The robustness of SD method enables a continuation or a gradual change on the degree of fitting function during the optimization, similar to the continuation scheme popular for SIMP interpolation [85]. This needs further exploration. Feature size control for manufacturability is a topic of practical interest.

Replication of Results

The MATLAB code used in this paper is available at www.ersl.wisc.edu/software/gMTO.zip.

Acknowledgments

The authors would like to thank the support of National Science Foundation through grant CMMI 1561899. Prof. Suresh is a consulting Chief Scientific Officer of SciArt, Corp.

Appendix A. Spectral decomposition of orthogonal-isotropic microstructures

For an orthogonal microstructure aligned along its axes of symmetry, the elasticity matrix components C_{13} and C_{23} are zero. Therefore, the third eigenvector $\boldsymbol{v}^{(3)}$ of orthogonal microstructure is always $\{0,0,1\}^{\mathsf{T}}$ with the corresponding eigenvalue $\lambda^{(3)} = C_{33}$. Thus, the SD of elasticity matrix can be expressed as

$$\boldsymbol{C} = \begin{bmatrix} C_{11} & C_{12} & 0 \\ C_{12} & C_{22} & 0 \\ 0 & 0 & C_{33} \end{bmatrix} = \begin{bmatrix} \boldsymbol{V}_{\mathrm{s}} & \boldsymbol{0} \\ \boldsymbol{0}^{\mathsf{T}} & 1 \end{bmatrix} \begin{bmatrix} \boldsymbol{\Lambda}_{\mathrm{s}} & \boldsymbol{0} \\ \boldsymbol{0}^{\mathsf{T}} & C_{33} \end{bmatrix} \begin{bmatrix} \boldsymbol{V}_{\mathrm{s}} & \boldsymbol{0} \\ \boldsymbol{0}^{\mathsf{T}} & 1 \end{bmatrix}^{\mathsf{T}}$$
$$\boldsymbol{C}_{\mathrm{s}} = \begin{bmatrix} C_{11} & C_{12} \\ C_{12} & C_{22} \end{bmatrix} = \boldsymbol{V}_{\mathrm{s}} \boldsymbol{\Lambda}_{\mathrm{s}} \boldsymbol{V}_{\mathrm{s}}^{\mathsf{T}} \tag{A.1}$$

where sub-matrices $\boldsymbol{C}_{\mathrm{s}}$, $\boldsymbol{V}_{\mathrm{s}}$ and $\boldsymbol{\Lambda}_s$ are the order 2 leading principal minors of elasticity matrix $\boldsymbol{C}$, eigenvector matrix $\boldsymbol{V}$, and diagonal eigenvalue matrix $\boldsymbol{\Lambda}$, respectively.

To ensure that eigenvectors are orthonormal, without loss of generality $\boldsymbol{V}_{\mathrm{s}}$ can be expressed using two scalars a and $b = \pm\sqrt{1-a^2}$ as

$$\boldsymbol{V}_{\mathrm{s}} = \begin{bmatrix} a & -b \\ b & a \end{bmatrix}$$

using Eqn. A.1,

$$\boldsymbol{C}_s = \begin{bmatrix} C_{11} & C_{12} \\ C_{12} & C_{22} \end{bmatrix} = \begin{bmatrix} a^2\lambda^{(1)} + b^2\lambda^{(2)} & ab\left(\lambda^{(1)} - \lambda^{(2)}\right) \\ ab\left(\lambda^{(1)} - \lambda^{(2)}\right) & a^2\lambda^{(2)} + b^2\lambda^{(1)} \end{bmatrix} \tag{A.2}$$

For orthogonal-isotropic microstructures, elasticity matrix components C_{11} and C_{22} are equal and therefore

$$\begin{aligned} a^2\lambda^{(1)} + b^2\lambda^{(2)} &= a^2\lambda^{(2)} + b^2\lambda^{(1)} \\ \implies \left(a^2 - b^2\right)\left(\lambda^{(1)} - \lambda^{(2)}\right) &= 0 \end{aligned}$$

using $b = \pm\sqrt{1-a^2}$,

$$a = \pm b = \pm\frac{1}{\sqrt{2}} \qquad \text{or} \qquad \lambda^{(1)} = \lambda^{(2)} \tag{A.3}$$

$$\implies \boldsymbol{C}_s = 0.5\begin{bmatrix} \lambda^{(1)} + \lambda^{(2)} & \mp\left(\lambda^{(1)} - \lambda^{(2)}\right) \\ \pm\left(\lambda^{(1)} - \lambda^{(2)}\right) & \lambda^{(1)} + \lambda^{(2)} \end{bmatrix} \qquad \text{or} \qquad \boldsymbol{C}_s = \lambda^{(1)}\begin{bmatrix} 1 & 0 \\ 0 & 1 \end{bmatrix} \tag{A.4}$$

The matrix on the right side corresponds to a zero Poisson's ratio microstructure and is a special case of matrix on the left side when the first and second eigenvalues are identical. Therefore, the elasticity matrix obtained by the left side matrix i.e.

$$\boldsymbol{C} = \begin{bmatrix} 0.5\left(\lambda^{(1)} + \lambda^{(2)}\right) & \mp 0.5\left(\lambda^{(1)} - \lambda^{(2)}\right) & 0 \\ \pm 0.5\left(\lambda^{(1)} - \lambda^{(2)}\right) & 0.5\left(\lambda^{(1)} + \lambda^{(2)}\right) & 0 \\ 0 & 0 & C_{33} \end{bmatrix} \tag{A.5}$$

represents the general elasticity matrix for orthogonal-isotropic microstructures with $\{1/\sqrt{2}, \pm 1/\sqrt{2}, 0\}^\mathsf{T}$, $\{\mp 1/\sqrt{2}, 1/\sqrt{2}, 0\}^\mathsf{T}$, and $\{0, 0, 1\}^\mathsf{T}$ as the eigenvectors.

Appendix B. Spectral decomposition of isotropic microstructures

An isotropic microstructure is a special case of orthogonal-isotropic microstructure for which the elasticity matrix remains invariant under rotational transformation. Therefore, we derive the condition for elasticity matrix given in Eqn. A.5 to be invariant under application of a rotation matrix given by

$$\boldsymbol{Q}(\theta) = \begin{bmatrix} \cos^2(\theta) & \sin^2(\theta) & \sin(2\theta) \\ \sin^2(\theta) & \cos^2(\theta) & -\sin(2\theta) \\ -\sin(2\theta)/2 & \sin(2\theta)/2 & \cos(2\theta) \end{bmatrix}$$

where θ is the angle of rotation of the microstructure. The rotated elasticity matrix is given by

$$\tilde{\boldsymbol{C}} = \boldsymbol{Q}(\theta)\boldsymbol{C}\boldsymbol{Q}^{\mathsf{T}}(\theta) \tag{B.1}$$

$$= \boldsymbol{Q}(\theta)\begin{bmatrix} 0.5\left(\lambda^{(1)}+\lambda^{(2)}\right) & \mp 0.5\left(\lambda^{(1)}-\lambda^{(2)}\right) & 0 \\ \pm 0.5\left(\lambda^{(1)}-\lambda^{(2)}\right) & 0.5\left(\lambda^{(1)}+\lambda^{(2)}\right) & 0 \\ 0 & 0 & C_{33} \end{bmatrix}\boldsymbol{Q}^{\mathsf{T}}(\theta) \tag{B.2}$$

$$= \boldsymbol{C} + \left(C_{33} - \frac{1}{4}\left(\left(\lambda^{(1)}+\lambda^{(2)}\right) \mp \left(\lambda^{(1)}-\lambda^{(2)}\right)\right)\right)\left(\sin(2\theta)\begin{bmatrix} \sin(2\theta) & -\sin(2\theta) & \cos(2\theta) \\ -\sin(2\theta) & \sin(2\theta) & -\cos(2\theta) \\ \cos(2\theta) & -\cos(2\theta) & -\sin(2\theta) \end{bmatrix}\right) \tag{B.3}$$

For $\tilde{\boldsymbol{C}}$ to be independent of rotation terms

$$C_{33} = \frac{1}{4}\left(\left(\lambda^{(1)}+\lambda^{(2)}\right) \mp \left(\lambda^{(1)}-\lambda^{(2)}\right)\right) \tag{B.4}$$

$$\implies C_{33} = \frac{\lambda^{(1)}}{2} \qquad \text{or} \qquad C_{33} = \frac{\lambda^{(2)}}{2} \tag{B.5}$$

Therefore, for elasticity matrix of isotropic microstructure the third eigenvalue $\lambda^{(3)} = C_{33}$ is always half of either the first or the second eigenvalue. Eigenvectors are same as that for the orthogonal-isotropic microstructures.

References

[1] M. P. Bendsøe, O. Sigmund, Topology optimization, Springer Berlin Heidelberg, 2004.

[2] O. Sigmund, K. Maute, Topology optimization approaches: A comparative review, Structural and Multidisciplinary Optimization 48 (6) (2013) 1031–1055.

[3] M. P. Bendsøe, Optimal shape design as a material distribution problem, Structural Optimization 1 (4) (1989) 193–202.

[4] M. Stolpe, K. Svanberg, An alternative interpolation scheme for minimum compliance topology optimization, Structural and Multidisciplinary Optimization 22 (2) (2001) 116–124.

[5] M. P. Bendsøe, N. Kikuchi, Generating optimal topologies in structural design using a homogenization method, Computer Methods in Applied Mechanics and Engineering 71 (2) (1988) 197–224.

[6] B. Hassani, E. Hinton, A review of homogenization and topology optimization I - Homogenization theory for media with periodic structure, Computers and Structures 69 (6) (1998) 707–717.

[7] J. A. Sethian, A. Wiegmann, Structural Boundary Design via Level Set and Immersed Interface Methods, Journal of Computational Physics 163 (2) (2000) 489–528. `arXiv:arXiv:1011.1669v3`.

[8] M. Wang, X. Wang, D. Guo, A level set method for structural topology optimization, Computer Methods in Applied Mechanics and Engineering 192 (1-2) (2003) 227–246.

[9] Y. M. Xie, G. P. Steven, A simple evolutionary procedure for structural optimization, Computers and Structures 49 (5) (1993) 885–896.

[10] X. Y. Yang, Y. M. Xei, G. P. Steven, O. M. Querin, Bidirectional evolutionary method for stiffness optimization, AIAA Journal 37 (11) (1999) 1483–1488.

[11] W. Zhang, J. Yuan, J. Zhang, X. Guo, A new topology optimization approach based on Moving Morphable Components (MMC) and the ersatz material model, Structural and Multidisciplinary Optimization 53 (6) (2016) 1243–1260.

[12] K. Suresh, A 199-line Matlab code for Pareto-optimal tracing in topology optimization, Structural and Multidisciplinary Optimization 42 (5) (2010) 665–679.

[13] S. Deng, K. Suresh, Multi-constrained topology optimization via the topological sensitivity, Structural and Multidisciplinary Optimization 51 (5) (2015) 987–1001.

[14] H. C. Rodrigues, J. M. Guedes, M. P. Bendsøe, Hierarchical optimization of material and structure, Structural and Multidisciplinary Optimization 24 (1) (2002) 1–10.

[15] Y. Wang, H. Xu, D. Pasini, Multiscale isogeometric topology optimization for lattice materials, Computer Methods in Applied Mechanics and Engineering 316 (2017) 568–585.

[16] W. Tao, M. C. Leu, Design of lattice structure for additive manufacturing, in: International Symposium on Flexible Automation, ISFA 2016, IEEE, 2016, pp. 325–332.

[17] Y. Wang, L. Zhang, S. Daynes, H. Zhang, S. Feih, M. Y. Wang, Design of graded lattice structure with optimized mesostructures for additive manufacturing, Materials and Design 142 (2018) 114–123.

[18] L. Cheng, X. Liang, J. Bai, Q. Chen, J. Lemon, A. To, On utilizing topology optimization to design support structure to prevent residual stress induced build failure in laser powder bed metal additive manufacturing, Additive Manufacturing 27 (March) (2019) 290–304.

[19] D. Li, N. Dai, Y. Tang, G. Dong, Y. F. Zhao, Design and Optimization of Graded Cellular Structures with Triply Periodic Level Surface-Based Topological Shapes, Journal of Mechanical Design, Transactions of the ASME 141 (7) (2019).

[20] F. Liu, Z. Mao, P. Zhang, D. Z. Zhang, J. Jiang, Z. Ma, Functionally graded porous scaffolds in multiple patterns: New design method, physical and mechanical properties, Materials & Design (2018).

[21] R. Sivapuram, P. D. Dunning, H. A. Kim, Simultaneous material and structural optimization by multiscale topology optimization, Structural and Multidisciplinary Optimization 54 (5) (2016) 1267–1281.

[22] T. Kumar, K. Suresh, A density-and-strain-based K-clustering approach to microstructural topology optimization, Structural and Multidisciplinary Optimization 61 (4) (2019) 1399–1415.

[23] Y. Zhang, H. Li, M. Xiao, L. Gao, S. Chu, J. Zhang, Concurrent topology optimization for cellular structures with nonuniform microstructures based on the kriging metamodel, Structural and Multidisciplinary Optimization 59 (4) (2019) 1273–1299.

[24] Y. Zhang, M. Xiao, H. Li, L. Gao, S. Chu, Multiscale concurrent topology optimization for cellular structures with multiple microstructures based on ordered SIMP interpolation, Computational Materials Science 155 (2018) 74–91.

[25] S. Daynes, S. Feih, W. F. Lu, J. Wei, Optimisation of functionally graded lattice structures using isostatic lines, Materials and Design 127 (2017) 215–223.

[26] C. Wang, J. H. Zhu, W. H. Zhang, S. Y. Li, J. Kong, Concurrent topology optimization design of structures and non-uniform parameterized lattice microstructures, Structural and Multidisciplinary Optimization 58 (1) (2018) 35–50.

[27] S. Arabnejad, D. Pasini, Mechanical properties of lattice materials via asymptotic homogenization and comparison with alternative homogenization methods, International Journal of Mechanical Sciences 77 (2013) 249–262.

[28] J. P. Groen, O. Sigmund, Homogenization-based topology optimization for high-resolution manufacturable microstructures, International Journal for Numerical Methods in Engineering 113 (8) (2018) 1148–1163.

[29] Y. Zhu, S. Li, Z. Du, C. Liu, X. Guo, W. Zhang, A novel asymptotic-analysis-based homogenisation approach towards fast design of infill graded microstructures, Journal of the Mechanics and Physics of Solids 124 (2019) 612–633.

[30] D. Xue, Y. Zhu, X. Guo, Generation of smoothly-varying infill configurations from a continuous menu of cell patterns and the asymptotic analysis of its mechanical behaviour, Computer Methods in Applied Mechanics and Engineering 366 (2020) 113037.

[31] A. D. Cramer, V. J. Challis, A. P. Roberts, Microstructure interpolation for macroscopic design, Structural and Multidisciplinary Optimization 53 (3) (2016) 489–500.

[32] G. Cheng, L. Xu, Two-scale topology design optimization of stiffened or porous plate subject to out-of-plane buckling constraint, Structural and Multidisciplinary Optimization 54 (5) (2016) 1283–1296.

[33] L. Cheng, J. Liu, X. Liang, A. C. To, Coupling lattice structure topology optimization with design-dependent feature evolution for additive manufactured heat conduction design, Computer Methods in Applied Mechanics and Engineering 332 (2018) 408–439.

[34] R. S. Kumar, D. L. McDowell, Generalized continuum modeling of 2-D periodic cellular solids, International Journal of Solids and Structures 41 (26) (2004) 7399–7422.

[35] X. Liu, V. Shapiro, Sample-based synthesis of two-scale structures with anisotropy, CAD Computer Aided Design 90 (2017) 199–209.

[36] C. Liu, Z. Du, W. Zhang, Y. Zhu, X. Guo, Additive Manufacturing-Oriented Design of Graded Lattice Structures Through Explicit Topology Optimization, Journal of Applied Mechanics 84 (8) (2017) 081008. arXiv:NIHMS150003.

[37] H. Y. Lei, J. R. Li, Z. J. Xu, Q. H. Wang, Parametric design of Voronoi-based lattice porous structures, Materials and Design 191 (2020) 108607.

[38] C. Li, H. Lei, Z. Zhang, X. Zhang, H. Zhou, P. Wang, D. Fang, Architecture design of periodic truss-lattice cellsfor additive manufacturing, Additive Manufacturing (2020) 101172.

[39] A. S. Phani, M. I. Hussein, Introduction to Lattice Materials, in: Dynamics of Lattice Materials, John Wiley & Sons, Ltd, Chichester, UK, 2017, pp. 1–17.

[40] H. Deng, L. Cheng, X. Liang, D. Hayduke, A. C. To, Topology optimization for energy dissipation design of lattice structures through snap-through behavior, Computer Methods in Applied Mechanics and Engineering 358 (2020) 112641.

[41] A. D. Cramer, V. J. Challis, A. P. Roberts, Physically Realizable Three-Dimensional Bone Prosthesis Design With Interpolated Microstructures, Journal of Biomechanical Engineering 139 (3) (2017) 031013.

[42] V. Challis, A. Cramer, A. Roberts, An optimised family of anisotropic microstructures with application to functionally graded materials, International Journal of Solids and Structures (may 2019).

[43] D. Pasini, S. Arabnejad, Elastostatics of Lattice Materials, in: Dynamics of Lattice Materials, John Wiley & Sons, Ltd, Chichester, UK, 2017, pp. 19–51.

[44] S. Sotiropoulos, G. Kazakis, N. D. Lagaros, Conceptual design of structural systems based on topology optimization and prefabricated components, Computers & Structures 226 (2020) 106136.

[45] E. Andreassen, C. S. Andreasen, How to determine composite material properties using numerical homogenization, Computational Materials Science 83 (2014) 488–495.

[46] A. C. Cameron, F. A. Windmeijer, An r-squared measure of goodness of fit for some common nonlinear regression models, Journal of econometrics 77 (2) (1997) 329–342.

[47] M. Jansen, O. Pierard, A hybrid density/level set formulation for topology optimization of functionally graded lattice structures, Computers & Structures 231 (2020) 106205.

[48] S. Watts, W. Arrighi, J. Kudo, D. A. Tortorelli, D. A. White, Simple, accurate surrogate models of the elastic response of three-dimensional open truss micro-architectures with applications to multiscale topology design, Structural and Multidisciplinary Optimization 60 (5) (2019) 1887–1920.

[49] T. Wu, K. Liu, A. Tovar, Multiphase topology optimization of lattice injection molds, Computers & Structures 192 (2017) 71–82.

[50] L. Cheng, J. Bai, A. C. To, Functionally graded lattice structure topology optimization for the design of additive manufactured components with stress constraints, Computer Methods in Applied Mechanics and Engineering 344 (2019) 334–359.

[51] L. Cheng, J. Liu, X. Liang, A. C. To, Coupling lattice structure topology optimization with design-dependent feature evolution for additive manufactured heat conduction design, Computer Methods in Applied Mechanics and Engineering 332 (2018) 408–439.

[52] C. Wang, X. Gu, J. Zhu, H. Zhou, S. Li, W. Zhang, Concurrent design of hierarchical structures with three-dimensional parameterized lattice microstructures for additive manufacturing, Structural and Multidisciplinary Optimization 61 (3) (2020) 869–894.

[53] D. Li, N. Dai, Y. Tang, G. Dong, Y. F. Zhao, Design and optimization of graded cellular structures with triply periodic level surface-based topological shapes, Journal of Mechanical Design 141 (7) (2019).

[54] Z. Wu, F. Fan, R. Xiao, L. Yu, The substructuring-based topology optimization for maximizing the first eigenvalue of hierarchical lattice structure, International Journal for Numerical Methods in Engineering 121 (13) (2020) 2964–2978.

[55] O. Sigmund, Materials with prescribed constitutive parameters: An inverse homogenization problem, International Journal of Solids and Structures 31 (17) (1994) 2313–2329.

[56] G. W. Milton, A. V. Cherkaev, Which elasticity tensors are realizable?, Journal of Engineering Materials and Technology 117 (4) (1995) 483.

[57] L. Cheng, P. Zhang, E. Biyikli, J. Bai, J. Robbins, A. To, Efficient design optimization of variable-density cellular structures for additive manufacturing: theory and experimental validation, Rapid Prototyping Journal (2017).

[58] H. P. Gavin, Strain Energy in Linear Elastic Solids CEE 201L. Uncertainty, Design, and Optimization, Tech. Rep. 2, Department of Civil and Environmental Engineering, Duke University (2015).

[59] W. Thomson, Xxi. elements of a mathematical theory of elasticity, Philosophical Transactions of the Royal Society of London 146 (1856) 481–498.

[60] M. M. Mehrabadi, S. C. Cowin, Eigentensors of linear anisotropic elastic materials, The Quarterly Journal of Mechanics and Applied Mathematics 43 (1) (1990) 15–41.

[61] S. Sutcliffe, Spectral Decomposition of the Elasticity Tensor, Journal of Applied Mechanics 59 (4) (1992) 762–773.

[62] P. Theocaris, T. Philippidis, Spectral decomposition of compliance and stiffness fourth-rank tensors suitable for orthotropic materials, ZAMM-Journal of Applied Mathematics and Mechanics/Zeitschrift für Angewandte Mathematik und Mechanik 71 (3) (1991) 161–171.

[63] P. Theocaris, T. P. Philippidis, Variational bounds on the eigenangle ω of transversely isotropic materials, Acta mechanica 85 (1-2) (1990) 13–26.

[64] P. S. Theocaris, D. P. Sokolis, Spectral decomposition of the linear elastic tensor for monoclinic symmetry, Acta Crystallographica Section A: Foundations of Crystallography 55 (4) (1999) 635–647.

[65] P. S. Theocaris, D. P. Sokolis, Spectral decomposition of the compliance tensor for anisotropic plates, Journal of elasticity 51 (2) (1998) 89–103.

[66] P. S. Theocaris, D. P. Sokolis, Invariant elastic constants and eigentensors of orthorhombic, tetragonal, hexagonal and cubic crystalline media, Acta Crystallographica Section A: Foundations of Crystallography 56 (4) (2000) 319–331.

[67] D. R. Jantos, K. Hackl, P. Junker, Topology optimization with anisotropic materials, including a filter to smooth fiber pathways, Structural and Multidisciplinary Optimization (2020) 1–20.

[68] D. R. Jantos, P. Junker, K. Hackl, Optimized growth and reorientation of anisotropic material based on evolution equations, Computational Mechanics 62 (1) (2018) 47–66.

[69] S. Czarnecki, T. Lewiński, The free material design in linear elasticity, in: Topology optimization in structural and continuum mechanics, Springer, 2014, pp. 213–257.

[70] S. Czarnecki, T. Lewiński, A stress-based formulation of the free material design problem with the trace constraint and multiple load conditions, Structural and Multidisciplinary Optimization 49 (5) (2014) 707–731.

[71] G. Dzierżanowski, T. Lewiński, Compliance minimization of thin plates made of material with predefined kelvin moduli. part i. solving the local optimization problem, Archives of Mechanics 64 (1) (2012) 21–40.

[72] G. Strang, Introduction to linear algebra, Vol. 3, Wellesley-Cambridge Press Wellesley, MA, 1993.

[73] W. H. Press, S. A. Teukolsky, W. T. Vetterling, B. P. Flannery, Numerical recipes 3rd edition: The art of scientific computing, Cambridge university press, 2007.

[74] O. Sigmund, Morphology-based black and white filters for topology optimization, Structural and Multidisciplinary Optimization 33 (4-5) (2007) 401–424.

[75] C. S. Jog, R. B. Haber, M. P. Bendsøe, Topology design with optimized, self-adaptive materials, International Journal for Numerical Methods in Engineering 37 (8) (1994) 1323–1350.

[76] E. Andreassen, A. Clausen, M. Schevenels, B. S. Lazarov, O. Sigmund, Efficient topology optimization in MATLAB using 88 lines of code, Structural and Multidisciplinary Optimization 43 (1) (2011) 1–16.

[77] M. T. Heath, Scientific Computing: An Introductory Survey, Revised Second Edition, SIAM, 2018.

[78] O. Rand, V. Rovenski, Analytical methods in anisotropic elasticity: with symbolic computational tools, Springer Science & Business Media, 2007.

[79] A. Chandrasekhar, T. Kumar, K. Suresh, Build optimization of fiber-reinforced additively manufactured components, Structural and Multidisciplinary Optimization 61 (1) (2020) 77–90.

[80] Z. D. Ma, N. Kikuchi, H. C. Cheng, Topological design for vibrating structures, Computer Methods in Applied Mechanics and Engineering 121 (1-4) (1995) 259–280.

[81] C. S. Jog, Topology design of structures subjected to periodic loading, Journal of Sound and Vibration 253 (3) (2002) 687–709.

[82] P. Yadav, K. Suresh, Large scale finite element analysis via assembly-free deflated conjugate gradient, Journal of Computing and Information Science in Engineering 14 (4) (2014).

[83] B. C. Prabhune, K. Suresh, A fast matrix-free elasto-plastic solver for predicting residual stresses in additive manufacturing, Computer-Aided Design (2020) 102829.

[84] T. Kumar, K. Suresh, Direct lagrange multiplier updates in topology optimization revisited, Structural and Multidisciplinary Optimization (in press) (2020).

[85] C. S. Jog, Variable-Topology Shape Optimization of Linear Elastic Structures, Ph.D. thesis, University of Illinois at Urbana-Champaign (1994).